Master Thesis

Vertical landing flight envelope definition

Definice letové obálky pro vertikální přistání

Jack Hooper

MASTER'S THESIS ASSIGNMENT

I. Personal and study details

Student's name: **Hooper Jack Charles**   Personal ID number: **489934**

Faculty / Institute: **Faculty of Electrical Engineering**

Department / Institute: **Department of Control Engineering**

Study program: **Cybernetics and Robotics**

Branch of study: **Cybernetics and Robotics**

II. Master's thesis details

Master's thesis title in English:

Vertical landing flight envelope definition

Master's thesis title in Czech:

Definice letové obálky pro vertikální přistání

Guidelines:

This project will define the complete space of system states for a launch vehicle (displacement, velocity, orientation) that will allow the vehicle to reach a desired end state upon landing. A model of the system dynamics and launch vehicle properties must be created to propagate the trajectory of the vehicle, which can be verified against existing re-entry software.
1) Get familiar with typical launch vehicles and missions.
2) Develop mathematical model of system dynamics and verify model against existing software.
3) Define the pace of landable states (Flight envelop definition).
4) Verify flight envelope based on simulations

Bibliography / sources:

[1] Ashish Tewari, Atmospheric and Space Flight Dynamics: Modeling and Simulation with Matlab and Simulink (Modeling and Simulation in Science, Engineering and Technology), Springer; 2007 edition (20 Dec. 2006)
[2] Jan Roskam , Airplane Flight Dynamics and Automatic Flight Controls: Airplane Flight Dynamics and Automatic Flight Controls, (2001, Paperback, Revised)
[3] Peter C Hughes, Spacecraft Attitude Dynamics, Dover Publications Inc. (28 Jan. 2005)

Name and workplace of master's thesis supervisor:

Ing. Tomáš Haniš, Ph.D.,   Department of Control Engineering,   FEE

Name and workplace of second master's thesis supervisor or consultant:

Date of master's thesis assignment: **28.01.2020**   Deadline for master's thesis submission: **14.08.2020**

Assignment valid until:
by the end of winter semester 2021/2022

_____   _____   _____
Ing. Tomáš Haniš, Ph.D.   prof. Ing. Michael Šebek, DrSc.   prof. Mgr. Petr Páta, Ph.D.
Supervisor's signature   Head of department's signature   Dean's signature

III. Assignment receipt

.
_____   _____
Date of assignment receipt   Student's signature

Acknowledgements

Declaration

I declare that I have worked out this thesis independently, assuming that the results of the thesis can also be used at the discretion of the supervisor of the thesis as its co-author. I also agree with the potential publication of the results of the thesis or of its substantial part, provided I will be listed as the co-author.

Abstract

This paper will investigate the development of a landing footprint for a re-entry vehicle. Vehicles can re-enter the atmosphere with a range of orientations, velocities and flight path angles. The central question is whether a vehicle with any combination of these states can be brought to an acceptable landing condition at a particular landing site and with a particular landing speed. To aide in this investigation several models must be implemented, including that of the atmosphere, the vehicles, the Earth, and the aerodynamics. A detailed analysis of the aerodynamic model will be treated, and the equations of motion subject to these aerodynamic laws will then be compared to results from existing atmospheric re-entry software. The principles of optimization will then be employed to generate the footprint of landable states, based on maximum and minimum possible downrange distances, for two vehicle concepts.

Keywords:

Abstrakt

Klíčová slova:

Překlad názvu: Definice letové obálky pro vertikální přistání

Contents

Figures

Tables

Chapter 1

Introduction

1.1 Background

Much of the early motivation for developing guidance and control for re-entry purposes began in the 1950s and was centered around militaristic capabilities, with the development of the intercontinental ballistic missile. When the focus of the US and the USSR shifted towards manned space exploration, interest in guidance and control entered into the civilian domain, and shortly afterwards NASA would develop interest in operating a reusable space plane, the Shuttle Orbiter, which would need to be guided through the upper atmosphere towards a landing runway.

In the 1960s a great deal of the theoretical framework for optimization as applied to re-entry and ascent cases was laid out. At the same time, improved aerodynamic models were being developed for rocket flight in the supersonic and high angle of attack flight regimes. In 1959, Miele applied the theory of calculus of variations to a ballistic missile equipped with a drag regulating device to minimize heat transfer during a re-entry case.[26] Shortly afterwards Breakwell, Speyer, and Bryson also used the theory of calculus of variations in the context of re-entry.[6] The first example they were concerned with consisting of thrust direction control to ascend a vehicle into a specific orbit. The second involved generating a family of optimal paths that would maximise final velocity, by varying the initial flight path angle by 0.2 degrees for a constant initial altitude and re-entry velocity. Bryson and Denham would then go on to incorporate inequality constraints into the optimal programming problem, integrating these features into the problem of finding a steepest ascent flight.[10] Many of the results of this early era were compiled by Vinh, who in 1981 published the textbook, Optimal Trajectories in Atmospheric Flight.[37]

The concept of a landing footprint, the reachable domain of all downrange

1

and cross-range locations a vehicle can be guided to was explored in the context of the Shuttle Orbiter, which was capable of a much more notable lateral range.[31] In this study, the multiple shooting method was applied to investigate the optimal trajectories of the vehicle.

The use of direct methods to solve optimal control re-entry problems became more common in the 90s, with the advent of more powerful computation. Whereas single shooting methods have found to be appropriate for ascent models, where thrust is the dominant force and the model is simpler and parameterised with fewer variables, they do not apply so well for more complicated re-entry scenarios. Hargraves and Paris in 1987 applied a direct collocation method by representing state variables with cubic Chebyshev polynomials.[17] Using these method, direct numerical solutions were found for the optical control problem of minimum-time supersonic climb. A few years later, Betts and Huffman improved upon this method by implementing methods to better handle problems with matrices that are large and sparse.[4]

In more recent history, there has been a shift towards re-entry guidance for vertical take-off, vertical landing (VTVL) vehicles. This has been inspired by the work done by engineers at Space X, who have developed the reusable first stage of the Falcon 9, as well as Blue Origin's development of the New Shepard for suborbital flight. An early study of a similar concept as the Falcon 9 was published by Ishijima, Matsumoto, and Hayashi who investigated guidance for a VTVL two stage to orbit vehicle using feedback control to modify the vehicle motion to a desired landing state[21]. Policelli has applied MATLAB's nonlinear programming solver FMINCON to optimize the trajectory of a VTVL vehicle to minimize propellant use while enabling a successful touchdown.[32]

■ 1.2 Project goals

The aim of this project is to define a space of system states for a launch vehicle (displacement, velocity, orientation), that will enable the vehicle to reach a desired end state upon landing. A model of the system dynamics and launch vehicle properties must be created to propagate the trajectory of the vehicle, which can be verified against existing re-entry software.

- Get familiar with typical launch vehicles and missions

- Develop mathematical model of system dynamics and verify model against existing software

- Define the space of landable states (flight envelope definition)

- Verify flight envelope based on simulations

1.3 Methodology

The space of landable states is defined as the combination of vehicle velocities, orientations, and starting positions that allow it to reach a desired end state. The most important qualities of this end state are the landing site's downrange distance, an altitude of close to zero, and an appropriate velocity and flight path angles. To constrain the number of states required for the envelope definition and to simplify the problem, the vehicle will be constrained to planar motion re-entry instead of the full range of three dimensional motion. In this sense, there will be only one flight path angle, γ, and only one aerodynamic angle, the angle of attack α.

For this problem the flight envelope can essentially be framed as being the landing footprint, so long as those additional end requirements for altitude, velocity, and flight path angle are also imposed. To define the landing footprint, the maximum and minimum possible downrange distances must be calculated. If, at the beginning of its re-entry, the vehicle is no further from the site than the maximum possible range and no closer to the site than the minimum possible range it is a state within the flight envelope.

Additionally, by assuming that the vehicle is only controlled in the atmosphere, below an altitude of 80km, and knowing that all re-entry vehicles must begin their descent at an altitude of above 80km, the problem can be further simplified. While the flight envelope will depend on the vehicle's initial altitude, in this case that initial altitude will always be 80km. If the vehicle flight were to be considered starting at a lower or higher altitude, this would also need to be considered. Additionally, as the flight trajectory will be the same irrespective of starting latitude, the footprint of the vehicle will also be the same. This means that the flight envelope must be generated only for a range of velocities and flight path angles.

The question of finding the maximum and minimum downrange distance is an optimization problem. To this end, an open source pseudo-spectral solver developed by Daniel R. Herber[19] will be used within MATLAB to find the maximum and minimum ranges for each velocity and flight path angle state combination. This problem will be solved for two vehicle types. The first is a vehicle analogous to the Shuttle Orbiter, which will land on a shallow glide path slope with a comparatively high final velocity. The second is analogous to the Ariane V liquid fly back booster (LFBB) concept developed by DLR, but which is modified to land vertically, touching down with a small velocity.[12]

A model of the system dynamics must be created to provide the dynamic constraint for the solver and to make the problem physically meaningful. Models of the Earth, atmosphere, and vehicle aerodynamics have been developed by implementing existing theory. In particular for the aerodynamic

3

model, the aerodynamic coefficients have been computed as a function of the Mach number, angle of attack, and control surface deflection by using semi-empirical relationships and experimental data valid across subsonic, supersonic, and hypersonic flight regimes and a full range of rotation. For much of the elaboration of this theory, the textbook Rocket Aerodynamics by Krasnov[23] alongside the 1978 revision of the DATCOM (United States Air Force Stability and Control Digital Data Compendium) manual have been used to provide the most relevant models to apply in this investigation.[20]

Chapter 2

Equations of motion

2.1   Reference frames

In order to describe the motion of a re-entry vehicle, it is useful to consider different coordinate systems in particular frames that are referenced to the direction of the different forces acting on the vehicle. This will simplify the process of resolving the component of force acting in the key reference frame used for the analysis, as rotation matrices can be used to simply transfer the force into a different coordinate system.

Coordinate systems of interest include:

- Body-fixed: Moves with the rotation of the vehicle. X towards vehicle nose, Z down, Y right.

- Wind-fixed: Moves with the trajectory of the vehicle. X in direction of velocity, Z down, Y right.

- Local horizon: Z from vehicle CG to Earth CG, X $\perp$ Z in plane of motion.

- ECF: Z towards north pole, X towards prime meridian, Y towards 90° E longitude.

- ECI: Earth centered like ECF but rotating with the Earth and referenced to the standard Epoch J2000, the orientation of the Earth at 12hr on Jan 1 2000.

Several methods of coordinate transformation exist, such as the direction cosine matrix, quaternions and Euler angles. Euler angles have the drawback of potentially introducing singularities into the system and involve non-linear equations although they have the advantage of requiring only three equations.
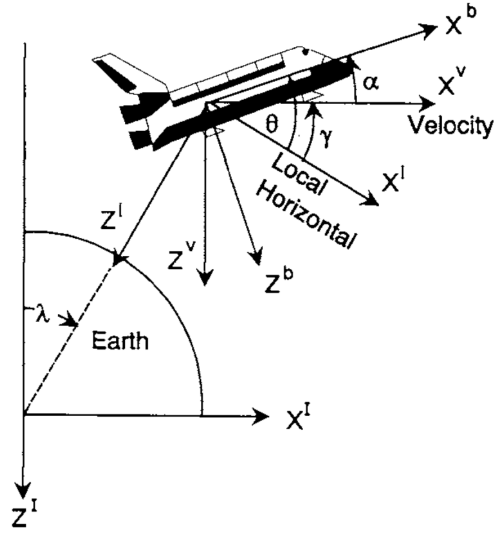
Figure 2.1: 2D representations of body, wind, local, and inertial coordinate systems.[33]

While quaternions do not introduce this singularity, they require a unity norm for pure rotation and this complicates the problem when attitude parameters, such as the angle of attack or flight path angle, are required to be optimised.[11] For this reason, the following Euler angle transformations can be used to convert between each coordinate system.

Body to local
about pitch angle Θ

$$C_l^b = \begin{bmatrix} \cos\Theta & 0 & -\sin\Theta \\ 0 & 1 & 0 \\ \sin\Theta & 0 & \cos\Theta \end{bmatrix}$$

Wind to local
about flight path angle γ

$$C_l^v = \begin{bmatrix} \cos\gamma & 0 & -\sin\gamma \\ 0 & 1 & 0 \\ \sin\gamma & 0 & \cos\gamma \end{bmatrix}$$

Inertial to local
about latitude θ

$$C_l^I = \begin{bmatrix} \cos\theta & 0 & -\sin\theta \\ 0 & 1 & 0 \\ \sin\theta & 0 & \cos\theta \end{bmatrix}$$

Body to wind
about angle of attack α

$$C_v^b = \begin{bmatrix} \cos\alpha & 0 & -\sin\alpha \\ 0 & 1 & 0 \\ \sin\alpha & 0 & \cos\alpha \end{bmatrix}$$

Derivative matrices $\Omega_{l/I}^v = \begin{bmatrix} 0 & 0 & \dot{\gamma} \\ 0 & 0 & 0 \\ -\dot{\gamma} & 0 & 0 \end{bmatrix}$

$\Omega_{v/l}^v = \begin{bmatrix} 0 & 0 & -\dot{\theta} \\ 0 & 0 & 0 \\ \dot{\theta} & 0 & 0 \end{bmatrix}$

It is conventional for orbital vehicles to be described by their Keplarian elements. In this case, these parameters must be converted into a re-entry coordinate system for use in the ensuing trajectory analysis. Additionally important context for the problem is gained through reference to the latitude and longitude of the vehicle as it travels over the Earth's surface. These

coordinates depend on the location of the vehicle in the reference plane but also the orientation of the plane relative to the ECI reference system. Transformations between these coordinate systems have been substantiated and then programmed into the problem solving environment.

To convert from ECF to ECI, the angular displacement with time from the vernal equinox is found as a relationship of the standard Epoch and angular velocity of the Earth.

$$\Omega = \omega_E(t - t_{J2000})$$

- $\omega_E = 7.29 \times 10^{-5} \frac{rad}{s}$

- t_{J2000} is the standard Epoch time

2.2 Equations of motion

For the purpose of simplifying this investigation, it will be assumed that the re-entry vehicle is confined to two dimensional motion within the plane prescribed by its initial suborbital trajectory. In this case, no sideforce can be experienced by the vehicle, and it must be assumed that the vehicle does not develop a sideslip with respect to the incoming wind. For this to be true, the vehicle must have the appropriate lateral control needed to attenuate any disturbances acting in this direction and must have be oriented with no sideslip at the beginning of any simulation.

The trajectory of a vehicle will be affected by gravitational, aerodynamic, and thrust force. The equation describing this interaction can be found through applying Newton's third law in the wind-fixed reference frame.

$$\frac{F_a^v}{m} + C_l^v \frac{F_g^l}{m} + C_b^v \frac{F_t^b}{m} = \dot{V}^v + \Omega_{v/I}^v V^v$$

$$\frac{F_g^l}{m} = \begin{bmatrix} 0 & 0 & g \end{bmatrix}$$

$$\frac{F_a^v}{m} = \begin{bmatrix} -\frac{D}{m} & 0 & -\frac{L}{m} \end{bmatrix}$$

$$\frac{F_t^b}{m} = \begin{bmatrix} \frac{T}{m} & 0 & 0 \end{bmatrix}$$

By applying the coordinate transformation matrices, a standard form for the equations of motion will emerge.[33]

$$
\begin{bmatrix} \dot{V} \\ 0 \\ 0 \end{bmatrix} + \begin{bmatrix} 0 & 0 & \dot{\gamma} - \dot{\theta} \\ 0 & 0 & 0 \\ -(\dot{\gamma} - \dot{\theta}) & 0 & 0 \end{bmatrix} \begin{bmatrix} V \\ 0 \\ 0 \end{bmatrix} = \frac{1}{m} \begin{bmatrix} -D + T\cos\alpha \\ 0 \\ -L - T\sin\alpha \end{bmatrix} + \begin{bmatrix} -g\sin\gamma \\ 0 \\ g\cos\gamma \end{bmatrix}
$$

The states of altitude and angular position can be found by considering the kinematic relationship between position and velocity.

$$
V^I = \frac{dR^I}{dt} = \frac{d}{dt}(C_l^I R^l) = C_l^I \left(\frac{dR^l}{dt} + \Omega_{l/I}^l R^l \right)
$$

$$
C_I^l V^I = C_v^l V^v = \frac{dR^l}{dt} + \Omega_{l/I}^l R^l
$$

$$
\begin{bmatrix} \cos\gamma & 0 & \sin\gamma \\ 0 & 1 & 0 \\ -\sin\gamma & 0 & \cos\gamma \end{bmatrix} \begin{bmatrix} V \\ 0 \\ 0 \end{bmatrix} = \begin{bmatrix} 0 \\ 0 \\ -\dot{h} \end{bmatrix} + \begin{bmatrix} 0 & 0 & -\dot{\lambda} \\ 0 & 0 & 0 \\ \dot{\lambda} & 0 & 0 \end{bmatrix} \begin{bmatrix} 0 \\ 0 \\ -(R_e + h) \end{bmatrix}
$$

The resulting equations that describe the trajectory of the vehicle are a series of four first-order, nonlinear differential equations.[33] It should be noted that a singularity is indeed present for $V = 0$.

$$
\frac{dV}{dt} = -\frac{D}{m} + \frac{T}{m}\cos\alpha - g\sin\gamma
$$

$$
\frac{d\gamma}{dt} = \frac{L}{Vm} + \frac{T}{Vm}\sin\alpha - \frac{g}{V}\cos\gamma + \frac{V\cos\gamma}{R_e + h}
$$

$$
\frac{dh}{dt} = -V\sin\gamma
$$

$$
\frac{d\theta}{dt} = \frac{V\cos\gamma}{R_e + h}
$$

For planar motion, the vehicle will only be able to rotate about the axis perpendicular to the plane. Rotation will be experienced primarily due to the presence primarily of aerodynamic moments. A gravitational moment will also exist if the vehicle experiences a large gravity field gradient.[33] Also, a thrust moment can arise when the thrust force is unbalanced or offset from the center of mass of the vehicle. These secondary contributions will be assumed to be negligible in this case.

$$
\frac{dq}{dt} = \frac{M_y}{I_{yy}}
$$

One of the benefits of planar analysis is that, with no sideslip and wings-level, a simple relationship between the pitch angle and angle of attack holds.[5]

$$\Theta = \alpha + \gamma$$

$$\omega_{b/l}^b = \begin{bmatrix} 0 & \dot{\Theta} & 0 \end{bmatrix} \qquad \omega_{l/I}^b = \begin{bmatrix} 0 & -\dot{\theta} & 0 \end{bmatrix}$$
$$\omega_{v/l}^b = \begin{bmatrix} 0 & \dot{\gamma} & 0 \end{bmatrix} \qquad \omega_{b/v}^b = \begin{bmatrix} 0 & \dot{\alpha} & 0 \end{bmatrix}$$

$$\omega_{b/I}^b = \begin{bmatrix} 0 & q & 0 \end{bmatrix}$$

$$\omega_{b/I}^b = \omega_{b/l}^b + \omega_{l/I}^b = \dot{\Theta} - \dot{\theta} = \dot{\alpha} + \dot{\gamma} - \dot{\theta} = q$$

$$\frac{d\alpha}{dt} = q + \frac{d\theta}{dt} - \frac{d\gamma}{dt}$$

▍ 2.3 Forces and moments

Now that the motion of the vehicle has been related to the forces that it will experience, work must be done to resolve the calculation of those forces.

The aerodynamic forces are estimated through the use of non-dimensional aerodynamic coefficients, which are intrinsic to the object under flow and its properties such as shape, orientation, compressibility effects, surface roughness, and more. This parameter is used to scale the product of dynamic pressure of the flow field and the area under pressure, resulting in a force magnitude. The lift is by convention perpendicular to the local wind and the drag in the direction of the local wind.

$$L = \tfrac{1}{2}\rho V^2 C_L S_{ref}$$
$$D = \tfrac{1}{2}\rho V^2 C_D S_{ref}$$
$$M = \tfrac{1}{2}\rho V^2 C_M S_{ref} l_{ref}$$

As the shape of the vehicle is constant through its simulated flight, then a functional dependence between the aerodynamic coefficient data and angle of attack, Mach number, and control surface deflection can be established.

$$C_L, C_D, C_M = f(\alpha, M, \delta)$$

Such a model does not account for Reynolds number effects from variations in flow turbulence, assuming that the flow is fully developed and turbulent

$(Re = 10^6 > Re_{cr})$ along the entire length of the vehicle for the entire simulation. It also does not account for the effect of temperature changes, which affect the boundary layer and pressure distribution of the flow.

Aerodynamic data has been tabulated for use for a range of experimental and prototype vehicles, such as the Lockheed Martin X-33, which was a precursor for the Shuttle Orbiter. For custom vehicles however, such as an Ariane 5 LFBB, experimental data has not been tabulated and CFD simulations are prohibitive. In this case, a precedent exists in the form of semi-empirical relationships and generalised aerodynamic models can be programmed and employed to find the aerodynamic data for a range of vehicles across a grid of M, α, and δ values.

The vehicles will thrust by combusting and then ejecting the accelerated propellant, imparting a reactive force to the vehicle that in the opposite direction. Additionally, the flow of propellant out of the vehicle creates a pressurised region that further pushes the vehicle forward. At lower stages of the atmosphere where atmospheric pressure is greater, this effect is less noticeable.

$$T = \dot{m}V_e + (P_e - P_0)S_{base}$$

The exhaust velocity can be found as the product of gravity at sea level and the specific impulse, a generalised factor that can compare how effectively fuel is converted into propulsive force. Additionally, in real conditions the thrust force may affect the centre of gravity of the vehicle and the jet exhaust will likely affect the base drag however these effects will not be considered.

$$V_e = I_{sp}g_0$$

10

Chapter 3

The physical model

3.1 Atmospheric model

The most comprehensive atmospheric model to data is the 1976 US Standard Atmosphere, which improves upon the 1962 model of the atmosphere in especially in the thermosphere (80 - 700km) and fringes of the exosphere up to 1000km.[3] In the lower atmosphere the atmosphere is treated as a homogeneous gas where barometric equations, linear and exponentially decreasing, can be used to model the density and pressure. At higher altitudes however, although gas molecules are present, the calculation of density is complicated by dissociation and diffusion, which result in altitude dependent bands of different molecular species. While a MATLAB program does exist to approximately calculate this standard atmosphere at each altitude, the integration techniques used especially in the high altitude regions are non-linear and computationally expensive.[25]

Instead a simple approximation of the atmosphere shall be applied, using the barometric approximations for density and pressure as a function of altitude, h.

$$\rho = \rho_0 e^{\left(\frac{-g_0 M h}{R T_0}\right)}$$

$$P = P_0 e^{\left(\frac{-g_0 M h}{R T_0}\right)}$$

For the standard atmosphere:

- $P_0 = 101325 Pa$

- $T_0 = 288.15 K$

- $rho_0 = 1.225 \frac{kg}{m}$

- $g_0 = 9.80665 \frac{m}{s^2}$

The universal gas constant, R, and molar mass of air are also constant with altitude.

- $R = 8.3144 \frac{Nm}{molK}$

- $M = 0.02896 \frac{kg}{mol}$

3.2   Earth model

The conventional model for the Earth is based on the 1984 World Geodetic System (WGS-84), which defines the Earth as an ellipsoid.[9] This has implications for positional data, especially in a longitude, latitude, altitude model as the shape of the ellipsoid will affect the reference lines of latitude and altitude for the same point in inertial space. It will also have implications on the gravity model of the Earth due to the non-uniform distribution of mass. Indeed other effects, such as differing regions of composition within the Earth, will also affect the gravity field. To account for this the 1996 Earth Gravitational Model (EGM96) has been developed, which relates the gravitational force to zonal harmonic terms and latitude position.[24] The field resolution for this model is proportional to the degree of the harmonic equation. For 55km resolution of the Earth's gravitational field, over 360 coefficients are necessary.[24]

To simplify this problem, a lower fidelity spherical Earth approximation will be considered, with a mean radius of 6360 km. In this case, the gravitational force is simply the inverse square of the distance of the spacecraft to the Earth's centre.

The Earth's rotation will not affect the location of the landing site, as it moves from under the vehicle. While this would be critical for trajectory optimization particularly for vehicles starting in orbit at high altitudes, this consideration has not been modelled by the equations of motion and should be included in future work.

$$F = \frac{GM_e m}{r^2}$$

The resulting gravitational acceleration referenced to altitude is therefore simple and computationally inexpensive.

$$g = \frac{GM_e}{(R_e + h)^2}$$

12

3.3 Vehicle model

Two types of vehicles will be considered for this study, to account for the two main re-entry scenarios for reusable space vehicles. The first is the space-plane concept, which represented the design philosophy towards reusability in the 1970s as realised in vehicles such as the Shuttle Orbiter and Buran. These space-planes featured large wings to introduce significant lift forces and enable an unpowered gliding descent, where the vehicle would be controlled by aerodynamic surfaces in the atmosphere, much like an ordinary aircraft.

A simplified model of the Shuttle Orbiter will be used to examine this case. The vehicle will be modelled as a cylindrical body with a spherically blunted nose, and a swept wing with flaps on both side. The Orbiter also has a vertical tail and horizontal stabilizer, but as the lateral dynamics are not considered, this will not be included in the model. Likewise, to simplify the process of obtaining aerodynamic coefficients, the wing glove and more complicated geometrical features such as the pods and canopy will not be included.
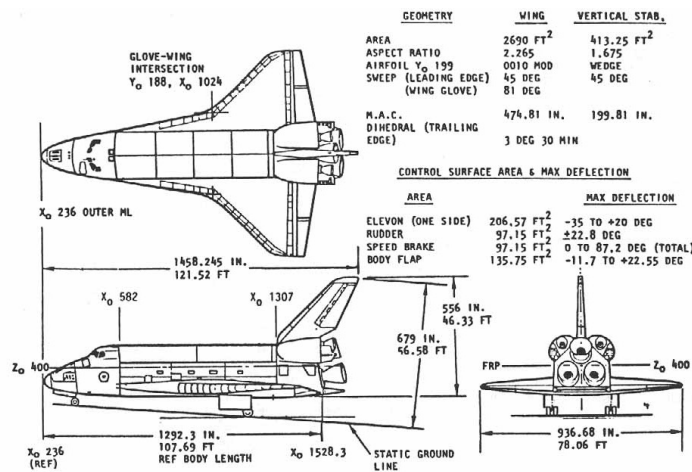
Figure 3.1: Detailed space shuttle schematic[30]

Shuttle model					
Wing			**Flaps**		
Wing span, b_w	23.79	m	Flap span b_f	8.87	m
Leading edge sweep, χ_{LE}	45	deg	Flap chord c_f	2.24	m
Root chord, c_r	17.51	m	Inboard flap location $b_{f,I}$	1	m
Tip chord, c_t	3.5	m	**Vehicle**		
Body			Total mass, m	99318	kg
Body diameter, d_b	6.5	m	Fuel mass, m_f	n/a	-
Nose length, l_n	3.7	m	Centre of gravity, X_{cg}	19	m
Forebody length, l_f	11.59	m			
Afterbody length, l_a	0	m			
Nose type	Blunt	-			
Nose blunting diameter, d_s	0.65	m			

The other type of vehicle will be a VTVL concept similar to the Falcon 9

boosters, where a combination of propulsive maneuvers and aerodynamic surfaces are used to control and land the vehicle. The European Space Agency, as part of its Future Launchers Preparatory Programme, has been investigating several reusable launch vehicle concepts. The Ariane 5 liquid fly-back booster (LFBB) concept[35] from this program will therefore be the second candidate vehicle to be tested. This vehicle is controlled through thrust vectoring and aerodynamic surfaces, but like all others in the programme, concludes with a horizontal landing on a runway. The vehicle will therefore assumed to be a modified form that is also fitted with vertical landing capabilities, so that the vertical landing case also can be considered.
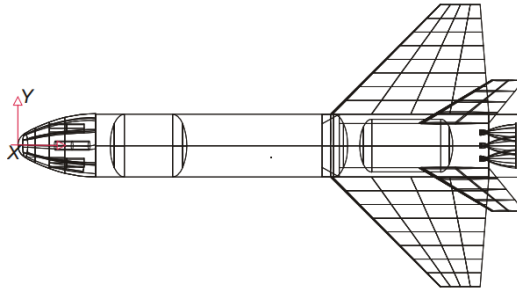
Figure 3.2: Ariane V LFBB schematic [35]

Ariane model					
Wing			**Flaps**		
Wing span, b_w	23.79	m	Flap span b_f	8.87	m
Leading edge sweep, χ_{LE}	45	deg	Flap chord c_f	2.24	m
Root chord, c_r	17.51	m	Inboard flap location $b_{f,I}$	1	m
Tip chord, c_t	3.5	m	**Vehicle**		
Body			Total mass, m	99318	kg
Body diameter, d_b	6.5	m	Fuel mass, m_f	n/a	-
Nose length, l_n	3.7	m	Centre of gravity, X_{cg}	19	m
Forebody length, l_f	11.59	m	**Engine**		
Afterbody length, l_a	0	m	Specific impulse	376	1/s
Nose type	Blunt	-	Exhaust pressure	36800	Pa
Nose blunting diameter, d_s	0.65	m	Max exhaust flow rate	235	kg/s

Chapter 4

Aerodynamic Model

4.1   Friction drag

The magnitude of skin friction drag is affected by turbulent effects and compressiblity effects. The point at which the flow will transition from laminar to turbulent is difficult to determine and depends on the critical Reynolds number, which varies from object to object, and the surface roughness. Generally for missiles in low atmosphere, this transition occurs on the nose cone. A simple estimation the critical transition length L can be considered with the general assumption that flow over elliptic bodies of revolution have a critical Reynolds number of 10^6.

$$Re = \frac{VL}{\nu}$$

The total friction drag can be resolved into the laminar $C_{D_{f,l}}$ and turbulent $C_{D_{f,tur}}$ drag before and after the critical point:

$$C_{D_f} = C_{D_{f,lam}}(x)\frac{S_x}{S_{ref}} + C_{D_{f,tur}}(L)\frac{S_L}{S_{ref}} - C_{D_{f,tur}}(x)\frac{S_x}{S_{ref}}$$

For laminar flow: $C_{D_{f,lam,0}} = \frac{1.328}{\sqrt{Re}}$ (Blasius)[23]

For turbulent flow: $\sqrt{C_{D_{f,tur,0}}}log_{10}(C_{D_{f,tur,0}}Re) = 0.242$ (Schoenherr)[23]

Compressibility effects:

For laminar flow: $C_{D_{f,lam}} = C_{D_{f,lam,0}}\left(1 + 0.17M^2\right)^{-0.1295}$

For turbulent flow: $C_{D_{f,tur}} = C_{D_{f,tur,0}}\left(1 + \frac{\gamma-1}{2}M^2\right)^{-0.467}$ (extended Frankl-Voishel)[16]

This approach to estimating the friction drag will be used for the wing and body in all flight regimes.

■ 4.1.1 Body Aerodynamics

■ Lift and moment

When treating slender bodies at an angle of attack, results can be obtained from the Allen-Perkins viscous cross-flow theory.[2] The premise of this theory is that the cross flow downstream is influenced only by the flow components perpendicular to the disturbing body, as was verified for laminar and turbulent experiments on yawed cylinders.

The potential flow has the following contribution.[2]

$$C_L = (k_2 - k_1)\frac{S_b}{S_{ref}}\sin 2\alpha \cos \frac{\alpha}{2}$$
$$C_{m_{CG}} = (k_2 - k_1)\frac{V - S_b(l - x_{cp})}{S_{ref}L_{ref}}\sin 2\alpha \cos \frac{\alpha}{2}$$

k_1 and k_2 represent the degree of axial and transverse mass moving as the angle of attack changes. For a sufficiently large fineness ratio it can be assumed that $k_2 - k_1 = 1$. [29]

When accounting for viscous effects, the circular cylinder at α will experience a force that must also be modelled. The coefficient of force C_{D_c} is dependent on the cross-flow Reynolds number and the cross-flow Mach number according to the following tables. It can be approximated as 1.1 for $Re = 10^4$ to 10^5 at $\alpha = 90^o$. The data given for C_{D_c} assumes an infinite 2D cylinder instead of a finite cylinder, and so this too must be corrected by the scaling factor η. Note that for the case of $\alpha = 0^o$ the body curvature is symmetric across the central streamline, an ellipsoid followed by a rectangle. The case of $\alpha = 90^o$ is approximated as potential flow around a circular cylinder. The resulting normal force in both cases is therefore zero.
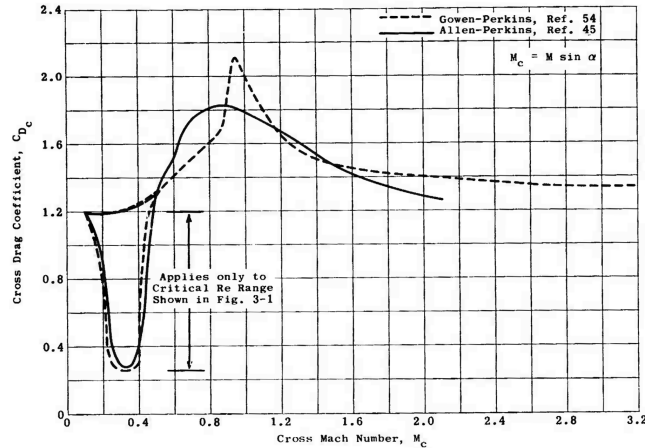
Figure 4.1: Cross flow drag coefficient
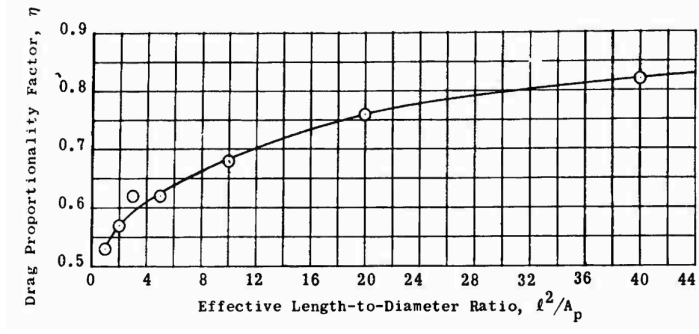
Figure 4.2: 3D cross flow drag correction factor

The viscous flow has the following contribution.[2]

$$C_L = \eta C_{D_c} \frac{S_p}{S_{ref}} \sin^2 \alpha$$
$$C_{m_{CG}} = \eta C_{D_c} \frac{S_p}{S_{ref}} \frac{x_m - x_p}{L_{ref}} \sin^2 \alpha$$

Now the effect of angle of attack on a slender inclined body can be considered by combining the potential cross-flow contribution yielded through slender body theory at small angles of attack combined with the vicious contribution as a result of larger angles of attack. [2]

$$C_L = (k_2 - k_1) \frac{S_b}{V_b^{\frac{2}{3}}} 2\alpha + \eta C_{D_c} \frac{S_p}{V_b^{\frac{2}{3}}} \alpha^2$$
$$C_{m_{CG}} = (k_2 - k_1) \frac{V - S_b(l - x_{CG})}{S_{ref} L_{ref}} 2\alpha + \eta C_{D_c} \frac{S_p}{S_{ref}} \frac{x_{CG} - x_P}{L_{ref}} \alpha^2$$

S_p is the planform area. For a cylinder, $S_p = 2 \int_0^l r(x)dx = 2rl$. S_b is the base area. For a cylinder, $A_b = \pi r^2$.

This principle towards finding the lift and pitching moment of the vehicle in the supersonic regime is the same, however to better fit experimental data in this region a simplified equation is suggested. In the transonic region a simple interpolation can be applied between the subsonic and supersonic values.[22]

$$C_L = 2\alpha + C_{D_c} \frac{S_p}{S_{ref}} \alpha^2$$
$$C_{m_{CG}} = 2\alpha(\frac{V_b}{S_b l_b} - (1 - \frac{x_{CG}}{l_b})) + C_{D_c} \frac{S_p}{S_b} \frac{x_{CG} - x_P}{l_b} \alpha^2$$

This relationship however breaks down in hypersonic flow. In this case, experimental test results as per figure 4.1, 4.2, and 4.3 can instead be used. The net moment is found by relating the center of pressure data to the center of gravity.[20]

17

$$C_{m_{CG}} = \left(\frac{X_{cg}}{l_b} - \frac{X_{cp}}{l_b} \right) C_{L_b}$$
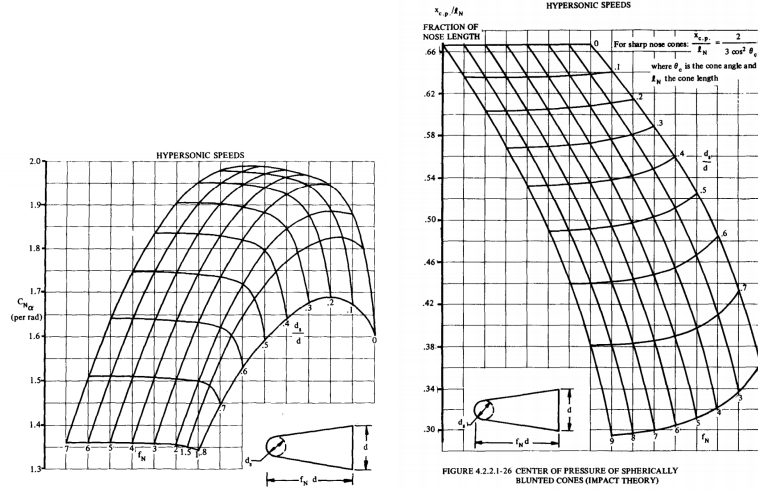
Figure 4.3: Lift and moment for conical nose[20]
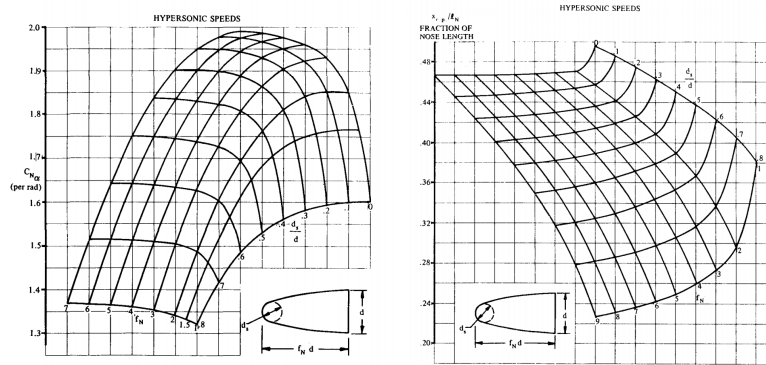
Figure 4.4: Lift and moment for ogive nose[20]
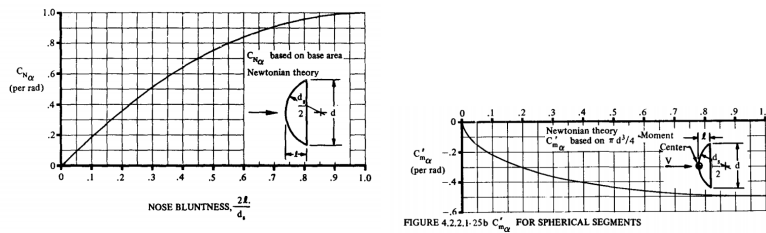
Figure 4.5: Lift and moment for spherical nose[20]

Pressure drag.   Pressure drag is created due to the normally resolved component of flow field pressure acting on the surface of a body. It is calculated by integrating these gradients in the direction of the relative wind. The shape of the object has a large effect on the degree of pressure drag experienced.

As the boundary layer flow develops along a surface, the shape of that surface will affect the velocity profile normal to the surface, leading to adverse pressure gradients and hence flow reversal. The subsonic pressure drag can be estimated as a ratio of the friction drag affected of course by the shape of the body. In the supersonic region this drag component is negligible.

$$C_{D_p} = C_{D_{f_B}}\left(\frac{60}{f_B^3} + 0.0025 f_B\right) \text{ [20]}$$

In the hypersonic regime pressure drag becomes dominant again, although the mechanism causing this is Newtonian impact theory. The coefficient in this regime can be calculated by interpolating experimental data.[20]
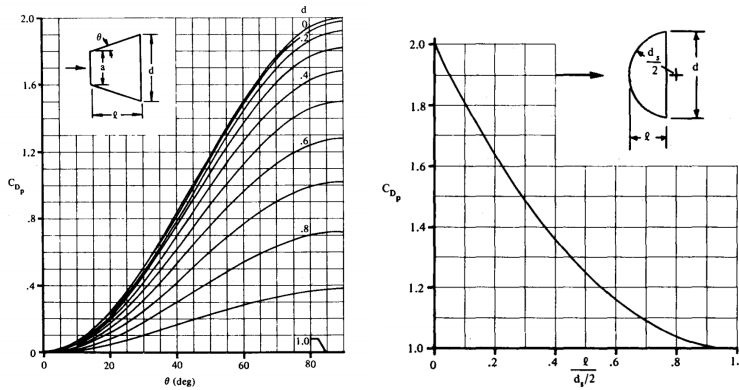
Figure 4.6: Hypersonic impact drag coefficient for a conical and blunted nose.[20]

Base drag. Base drag is caused by the separation when the flow meets the abrupt change of shape at the abruptly squared off base of the object. The resulting region of dead air aft of the base is then effectively pumped away by the incoming upstream flow, resulting in a region of lower pressure. For subsonic and low supersonic regimes, the base drag can contribute up to half of the total drag on the vehicle and so cannot be neglected. With higher Mach number, the proportional effect of base drag reduces. The limiting pressure at the base is one atmosphere, whereas the wave pressure can become much higher than one atmosphere due to the mechanics of the shock.

In the subsonic regime the base drag is a function of the friction and pressure drag. In the transonic, supersonic, and hypersonic regime, experimental data can be used to calculate the drag.

$$C_{D_b} = \frac{0.029}{\sqrt{C_{D_f} + C_{D_p}}}[?]$$

19
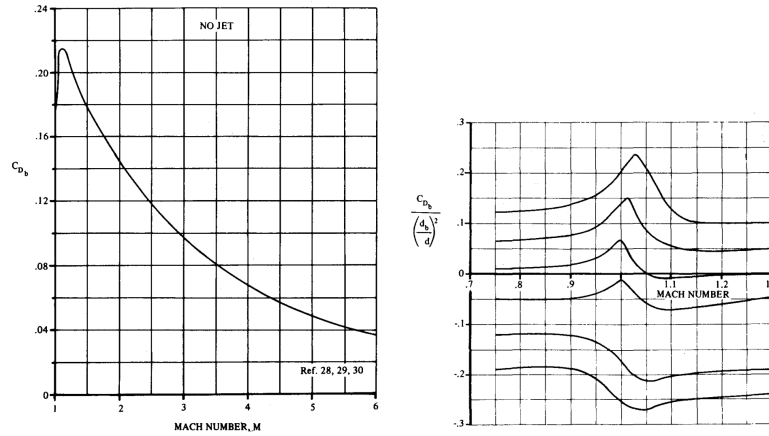
[20]

Figure 4.7: Base drag calculation in the subsonic (left) and transonic (right) regime.

Wave drag. At transonic and supersonic speeds shock-waves are produced leading to a pressure difference across the shock. This difference is characterised as the wave drag. In the range $1 < M < 3$ for bodies with moderate boattailing and slender noses, the wave drag is typically one-tenth to one-fourth of the total drag. The approach to estimating this drag involves calculating pressure distributions and shock geometries around particular bodies, and then integrating the distribution to find the total drag.

Conical nose

For a cone in supersonic flow, typically the flow-field has been evaluated through what is now known as the Taylor-Maccoll analysis. The assumption in this method is to approximate the flow as being potential to numerically integrate the flow properties along each axisymmetric conical ray. The result was tabulated data valid for 5 to 50 degree semi-vertex cone angles and all Mach numbers. When the flow viscosity is non-negligible or the gas non-ideal, then the data must be modified accordingly. The effect of the cylinderical afterbody on the downstream pressure distribution was examined by Clippinger, Giese, and Carter[8], who found that the pressure is restored to the freestream value, more gradually with increasing Mach number. The treatment for this downstream flow regime is typically to consider the flow as Prandtl-Meyer and conduct the analysis resultantly. The following empirical equation models this data, where σ is the semivertex cone angle in degrees, with 5% accuracy for $\sigma < 50^o$.

$$C_{D_{p,cone}} = \left(0.083 + \frac{0.096}{M^2}\right)\left(\frac{\sigma}{10}\right)^{1.69}$$

Ogival nose

Ehret, Rossow, and Steven[13] have developed analogously a table of pressure distributions for a ogive shaped nose with cylindrical afterbody. In this case, the method of characteristics and hypersonic similarity parameter were used to determine the results, with a later correction to account for the effects of flow rotation. A semi-empirical expression provided by EC Miles[27] links the drag on an ogive nose to that of a conical nose for an equivalent semi-vertex angle. Likewise Zienkewicz has developed a similar semi-empirical equation which is valid for the range $\frac{c}{d} \leq 2, M \geq 1.6, \frac{Md}{c} \leq 1$[38]

$$C_{D_{p,ogv}} = C_{D_{p,cone}} \left(1 - \frac{2(196(\lambda_f)^2 - 16)}{28(M+18)(\lambda_f)^2} \right)$$
$$C_{D_{p,ogv}} = C_{D_{p,cone}} \left(0.326 + 0.674 \left(1 - \frac{l}{c} \right)^{1.8} \right)$$
$$\sigma = \tan^{-1} \left(\frac{1}{2\lambda_f} \right)$$

$\lambda_f = \frac{l}{d}$ is the fineness ratio of the nosecone.

Bluntness drag. A blunt nose is a common nose shape for re-entering bodies (including the Shuttle), but calculating the drag at supersonic Mach numbers is complicated by the fact that the shape of the nose violates the small perturbation assumption which is fundamental in much of the study of supersonic nose cones. As theoretical approaches are more complicated, especially when the shape of shocks on the nose are unknown, the typical approach is to use experimentally derived pressure distributions and semi-empirical relationships. The bluntness drag will be estimated using experimental data.[20]
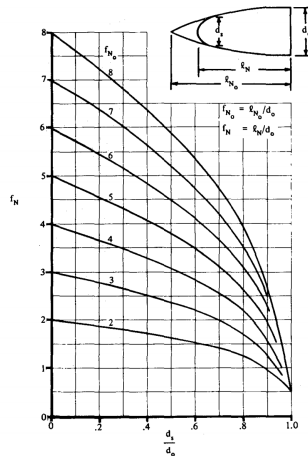
Figure 4.8: Bluntness drag for a spherically blunted ogive nosecone.[20]

4.2 Wing Aerodynamics

4.2.1 Subsonic

Wing lift. For a wing experiencing compressible flow, the lift coefficient as a function of angle of attack is a modification of the thin airfoil theory to introduce dependency on the Mach number.

$$C_L = \frac{C_{L_\alpha}(\alpha - \alpha_0)}{\sqrt{1-M^2} + \frac{C_{L_\alpha}}{AR\pi}(1+\tau)}$$

- AR: the wing aspect ratio.

- τ: parameter accounting for wing planform shape and taper, λ.

$\tau = 5.88\tau_1(m)\tau_2(\lambda)$ where for compressible flow $m = \frac{AR\sqrt{1-M^2}}{C_{L_\alpha}}$ [23]

```
TABLE V-1-2. THE COEFFICIENTS δ AND τ [6]

              Rectangular wings (η = 1)
```

λ_{wg}/a_0	1/2	3/4	1	1.25	1.5	1.75
δ	0.019	0.034	0.049	0.063	0.076	0.088
τ	0.10	0.14	0.17	0.20	0.22	0.24

```
                 Trapezoidal wings
```

η	1	4/3	2	4	∞
δ	0.049	0.026	0.011	0.016	0.141
τ	0.17	0.10	0.03	0.01	0.17

```
Note: The data from trapezoidal wings were obtained for
the condition that λ_wg = a_0.
```

Figure 4.9: Tabulated correction factors for wing[23]

The lift slope curve C_{L_α} describes the change of lift with angle of attack as a function of angle of attack. For a thin airfoil this can be assumed to be a constant, 2π. The zero-lift angle of attack α_0 is the angle of attack when no lift is being generated. For a symmetrical aerofoil this can be assumed to be at 0°. In general, both C_{L_α} and α_0 depend on the shape of the airfoil, its camber and thickness. These values can be extracted for particular 2D airfoil shapes using simulation software such as Javafoil.[18] Javafoil is only useful in the subsonic regime and only uses a simple potential flow theory to yield results, not accounting for inviscid effects like turbulent separation. In

this sense Javafoil is also not very useful beyond the stall angle for an airfoil, although approximations are provided.[18]
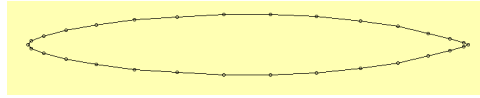
Figure 4.10: Shape of symmetrical airfoil to be used for both vehicles.
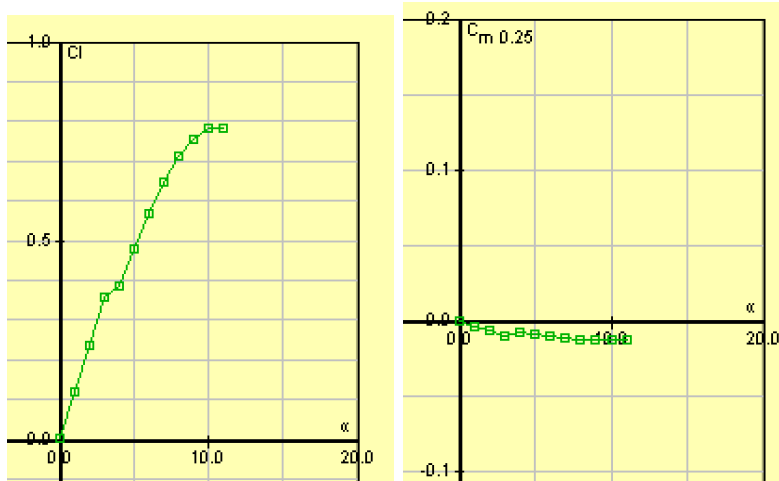
Figure 4.11: Polar for this airfoil.

When considering a wing with sweep, χ, the equation can be further modified, where τ_χ is evaluated with $m_\chi = \frac{AR}{C_{L_\alpha}\cos\chi}$.[23]

$$C_L = \frac{\pi AR(\alpha - \alpha_0)}{1 + \tau_\chi + \sqrt{(1+\tau_\chi)^2 + \frac{\pi^2 AR^2}{C_{L_\alpha}^3}(1 + \tan^2\chi - M^3)}}$$

Wing drag.   The subsonic wing drag is a combination of profile and induced drag. The profile drag is a function scales with the friction drag, increasing for thicker airfoils.[20]

$$C_{D_p} = C_{D_f}(\bar{t} + 100\bar{t}^4)$$

The induced drag is a function of the lift coefficient.[23]

$$C_{D_i} = \frac{C_L^2}{\pi AR\sqrt{1-M^2}}(1 + \delta)$$

$\delta = 20.41\delta_1(m_\chi)\delta_2(\lambda)$ where $m_\chi = \frac{AR}{C_{L_\alpha}\cos\chi}$ and δ is calculated in the same way as τ.

23

Wing pitch. In the subsonic regime, Javafoil can be used to estimate the wing pitching moment about the aerodynamic centre, a point on the wing that does not change with increasing angle of attack below stall. It also provides the location of the aerodynamic centre for the airfoil.

This can then be corrected for sweep effects by applying the following equation, and for compressibility effects by applying a compressibility factor.[20]

$$C_{m_{AC}} = C_{m_{AC,0}} \frac{AR \cos^2 \chi_{25}}{AR + 2\cos \chi_{25}}$$
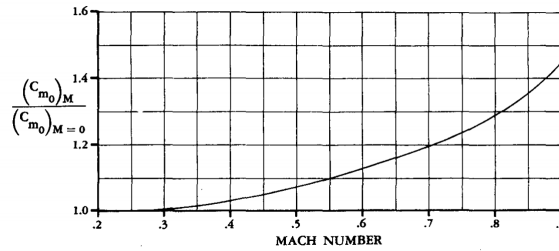
Figure 4.12: Wing moment compressiblity correction factor.[20]

This wing moment will be considered to be the same also in the transonic and supersonic regime. This can be converted to the moment at the centre of gravity of the vehicle.

$$C_{m_{CG}} = C_{m_{AC}} + L(x_{CG} - x_{AC})$$

▪ 4.2.2 Transonic

In the transonic region, the use of transonic similarity rules can be applied to calculate the lift and drag. For the lift, the wing thickness similarity parameter must first be calculated and then from this, the ratio of subsonic lift at the critical Mach number to the supersonic lift. [23]

$$\frac{\bar{t}_{cr}}{t} = \frac{M_{cr}^2 \sqrt{1-M^2}^{\frac{3}{2}}}{M^2 \sqrt{1-M_{cr}^2}^{\frac{3}{2}}}$$

$$\frac{C_{L_w}}{C_{L_{w,sub}}} = \frac{\bar{t}_{cr}}{t} \left(\frac{\sqrt{1-M_{cr}^2}}{\sqrt{1-M^2}} \right)$$

The drag in this regime is a combination of wave drag and induced drag. For wave drag, the result will be interpolated between 0 at the critical Mach number and the supersonic result at the supersonic Mach number.

The aerodynamic centre location can be found from experimental data in the transonic region, as a function of wing taper, aspect ratio, sweep, and Mach number. The moment at the aerodynamic centre is the same as per the subsonic case.

Figure 4.13: Aerodynamic centre location in transonic flow.

■ 4.2.3 Supersonic

To find the general pressure distribution of a generalised wing section, we can assume it is a sharp object and use the method of characteristics and the Prandtl-Meyer equations.[23] For this analysis the wing must be treated as 2D with no separation of boundary layer of shock, limiting α to below 10°. Corrections for finite span wings will be introduced later in the section, and a very simplified treatment of high angle of attack aerodynamics will also be considered later. The resulting pressure distribution is a series expansion of the shock angle (and so the slope of the upper and lower wing contours), altered by Mach dependent Busemann constants, C_1, C_2.

The Mach cone semi-vertex angle is a function of only free-stream Mach number. $\mu_M = \sin^{-1}(\frac{1}{M})$

Infinite span wing.

$$C_1 = \frac{1}{\sqrt{M^2 \cos^2 \chi - 1}}$$
$$C_2 = \frac{(M^2 \cos^2 \chi - 2)^2 + kM^4 \cos^4 \chi}{4(M^2 \cos^2 \chi - 1)^2}$$

For second order (non-linear) flow for a thin but not flat airfoil, the aerodynamics are as follows. The drag term consists of the effect of thickness and angle of attack on the wave drag, and in this sense it is lift dependent like induced drag. It does not account for flow circulation at the end of the wing tips that primarily causes the induced drag effect. [36]

$$C_L = 4C_1\alpha - 4C_1\alpha_0$$
$$C_D = \alpha C_L - 8C_2\alpha A_2 + 2C_1 B_2 - 2C_2 A_3$$

The terms A_2, A_3, B_2 account for the airfoil profile.

$$A_2 = \int_0^1 \left(\frac{dt_l}{dc}\right)^2 - \left(\frac{dt_u}{dc}\right)^2 dx$$
$$B_2 = \int_0^1 \left(\frac{dt_l}{dc}\right)^2 + \left(\frac{dt_u}{dc}\right)^2 dx$$
$$A_3 = \int_0^1 \left(\frac{dt_l}{dc}\right)^3 + \left(\frac{dt_u}{dc}\right)^3 dx$$

Correcting for finite span. With a finite span wing in three dimensional flow, the aerodynamics must be modified to compensate for the effect of the Mach cone formation. To correct for these effects, the wing is treated as a flat plate with sources and sinks introduced to model the three dimensionality of the flow. Tip flow and the resulting loss of lift will occur for the part of the wing not submerged within the Mach cone, which depends on the wing span. It will be assumed that always either the flow over the wing is entirely supersonic or that $\lambda_{wg} > \frac{1}{\sqrt{M^2-1}}$ to prevent Mach cones forming over each tip or to prevent them overlapping, which would further complicate the flow.

Results from Evvard's analysis will be used to correct the aerodynamic properties in the case of a finite span rectangular wing.[15] This is relevant only when the wing tips are not in the region contained by the Mach cone. Otherwise the flow field conforms to the two-dimensional flow substantiated in the above section.

$$C_L = 4C_1\alpha - \frac{4C_1\alpha}{2\lambda_{wg}\sqrt{M^2 \cos^2 \chi - 1}}$$
$$C_D = \alpha C_L$$

For the simple delta wing, however an analogous correction can be derived accounting for the different geometry. This follows methods outlined by Puckett and Stewart and assumes the wing has a low aspect ratio such that $\mu \gg \epsilon$ where ϵ is the sweep angle of the delta wing.[7]

The parameter $E(k)$, a function of Mach cone angle and sweep angle, is useful for determining the limiting cases.

$$E(k) = \sqrt{1 - \frac{\tan \epsilon}{\tan \mu}}$$

$$C_L = \frac{2\pi \frac{\tan \epsilon}{\tan \mu}}{E(k)\sqrt{M^2 \cos^2 \chi - 1}}$$
$$C_D = \alpha C_L - \frac{C_L^2}{\pi \lambda_{wg}} \sqrt{1 - \alpha' t_o^2}$$

When the wing leading edge is sonic $\alpha' t_o^2 = 1$ and so $E(k) \to \frac{\pi}{2}$

$$C_D = \frac{C_L^2}{\lambda_{wg}}$$

When the wing leading edge is supersonic $\alpha' t_o^2 \to 0$ and so $E(k) \to 1$

$$C_D = \frac{C_L^2}{\pi \lambda_{wg}}$$

The aerodynamic centre location can be found from experimental data in the supersonic region, as a function of wing taper, aspect ratio, sweep, and Mach number. The moment at the aerodynamic centre is the same as per the subsonic case.[20]
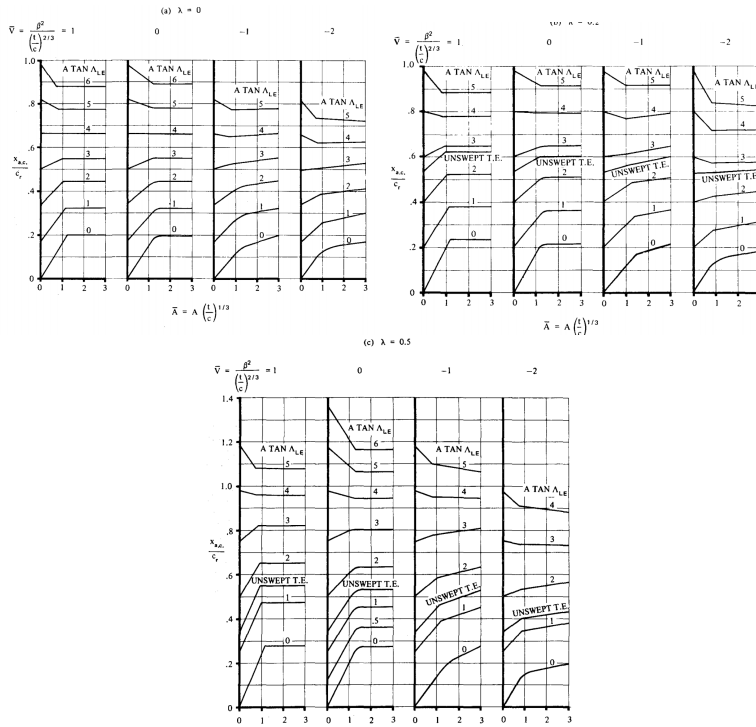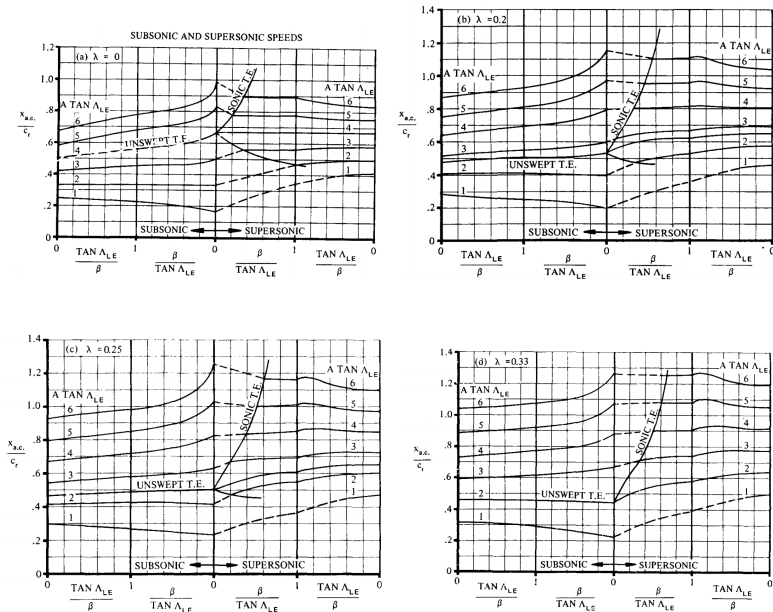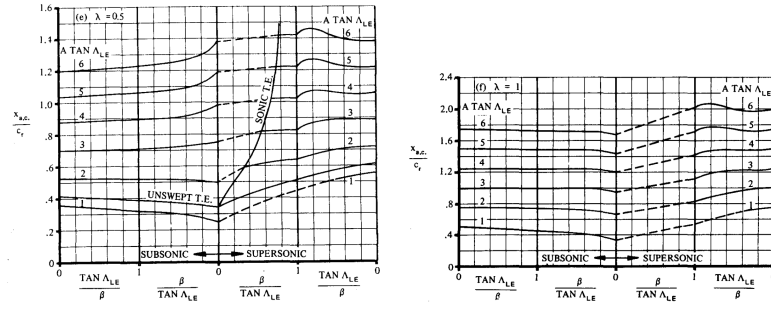
Figure 4.14: Aerodynamic centre location in supersonic flow.[20]

■ 4.2.4 Hypersonic

In the hypersonic regime corrections must be made to account for the thermo-dynamic effects of the gas. The first consideration must be whether the flow can still be treated as an ideal gas. If it is, there must also be a consideration of the mean free path of the particles relative to the boundary layer of the flow. When the mean free path is greater than the boundary layer, the gas must be treated as many discrete particles instead of a continuum flow. Newtonian impact theory shall be applied in this case.

At higher temperatures, and certainly above 2700K, molecules dissociate, ionise, and become more chemically active. In this case the fluid must be treated as a real gas. The ratio of specific heats will depend on the chemical interactions which can be modelled, and analysis methods must be non-isentropic to account for changes in entropy. The method of characteristics is one such method and is often applied to this problem.

In cases when the vehicle is at very high Mach numbers ($M \rightarrow \infty$), a likely scenario for the orbital speed at initial phases of re-entry. In this case, the lift and drag are caused by individual particles in the atmosphere colliding with the vehicle rather than a continuous flow, with momentum transferred as the particle rebounds from the surface. This is known as Newtonian impact theory. This theory only applies for the positive sloped contour of the wing, so the wing profile downstream of the surface point tangential to the flow will not be considered. Here the pressure is considered to be zero.

The angle β is measured between the tangent to the surface and the chord. The angle β_p is likewise but taken at the nose.

$$\beta = \tan^{-1}\left(\frac{dy}{dx}\right)$$
$$\beta_p = \tan^{-1}\left(\frac{dy_{(x=0)}}{dx}\right)$$

The pressure on each surface is then calculated assuming a shock for a flat plate.[23]

$$\bar{p}_u = (k+1)(\beta_u - \alpha)^2$$
$$\bar{p}_l = (k+1)(\beta_l - \alpha)^2$$

The lift and wave drag can then be found.

$$C_L = \int_0^{x_l} \bar{p}_l dx - \int_0^{x_u} \bar{p}_u dx$$
$$C_{D_P} = \alpha C_L - \int_0^{x_l} \bar{p}_l \bar{\beta}_l dx - \int_0^{x_u} \bar{p}_u \bar{\beta}_u dx$$

The moment coefficient at the leading edge can also be found and used to find the moment coefficient at the centre of gravity. [23]

$$C_{m_{LE}} = - \int_0^{x_l} \bar{p}_l \bar{x}_l dx + \int_0^{x_u} \bar{p}_u \bar{x}_u dx$$

4.3   Wing-body interactions

For many aircraft, and especially those with wingspans small compared to the body diameter, (the low aspect ratio shuttle, fins on a missile) there will be an interference effect between the lifting surfaces and the body. This means that a simple sum of the lift and drag from each component will not be equal to the total vehicle lift and drag. A tilting cylinder will have an upwash effect on the wing, as the generation of fluid motion normal to the body increases the local wing angle of attack. Wing vortices, caused by interaction of the flow with the wing tips, will result in an upwash forward of the lifting surface and a downwash aft of the surface. This will affect primarily the pitching moment of the cylindrical body. In cases where there are multiple lifting surfaces with the same orientation to the flow, an interference effect will also occur on the more aft surfaces (wing-wing interactions). For this study it is assumed surfaces at different positions on the length of the rocket body will also be in different planes of orientation. In other words, no vehicle will have an aft horizontal stabilizer to be effected by downwash effects. The space shuttle does however have a aft vertical stabilizer oriented at 90° to the wing surface. Induced aerodynamic forces will arise on this surface due to the wing, but as a vertical stabilizer does not produce lift or pitching moment this is not relevant in a discussion about the vehicle's longitudinal dynamics.

Lift.   For a wing at low angle of attack with zero incidence, K_{WB} is the effect of the body on the wing, K_{BW} is the effect of the wing on the body and can be determined from experimental data.[20]

$$C_{L_{WB}} = (K_N + K_{WB} + K_{BW})C_{L_\alpha}\alpha$$
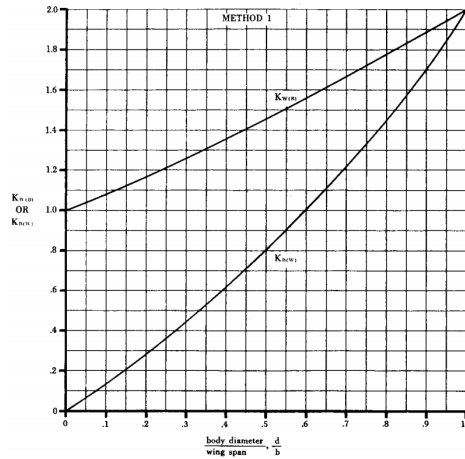
Figure 4.15: K_{WB} and K_{BW} standard data.[20]

For a delta wing in supersonic flight, if $AR\sqrt{M^2 - 1} \leq 1$ the data is the same as the subsonic case. For non-triangular wings this occurs when $AR\sqrt{M^2 - 1}(1 + \lambda)\left(\frac{\tan\chi}{\sqrt{M^2-1}} + 1\right) \leq 4$. Otherwise, experimental data that has modified the parameter K_{BW} to model the supersonic effect must be used instead of the subsonic data.
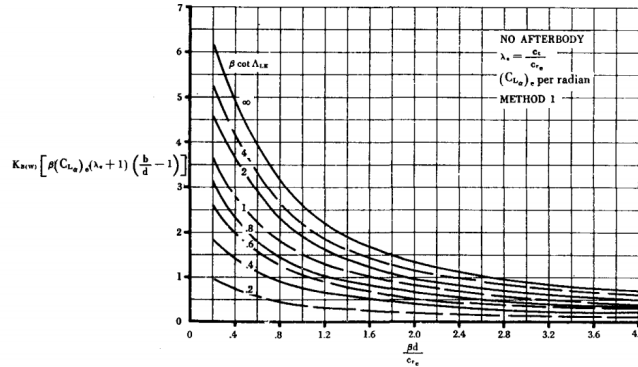
Figure 4.16: K_{BW} supersonic modified data.[20]

The interference parameter for the nose can be found from the following semi-empirical relationship, where S_N is the nose reference area, typically πr^2 and $C_{L_{\alpha,N}}$ is the nose lift curve slope, typically 2 per radian.

$$K_N = \frac{C_{L_{\alpha,N}} S_N}{C_{L_\alpha} S_W}$$

Drag. The total drag on the vehicle is the simple summation of each component, by scaled as to be referred to a common reference area.

$$C_{D_{o,wb}} =$$
$$(C_{D_{f,wg}} + C_{D_{p,wg}} + C_{D_{w,wg}} + C_{D_{i,wg}})\frac{S_w}{S_{ref}} + (C_{D_{f,b}} + C_{D_{p,b}} + C_{D_{w,b}})\frac{S_s}{S_{ref}} + C_{D_{b,b}}\frac{S_b}{S_{ref}}$$

Pitching moment. While the pitching moment at the aerodynamic centre is not affected by wing-body interference, the location of the aerodynamic centre on the body will be.[20] This is significant, as this location is required to find the total pitching moment at the centre of gravity.

The total aerodynamic centre is the weighted average of the aerodynamic centre of the wing adjusted for body interference, the body adjusted for wing interference, and the interference lift created on the nose.

$$\frac{x_{ac}}{c_r} = \frac{\left(\frac{x_{ac}}{c_r}\right)_n C_{L\alpha,n} + \left(\frac{x_{ac}}{c_r}\right)_{wb} C_{L\alpha,wb} + \left(\frac{x_{ac}}{c_r}\right)_{bw} C_{L\alpha,bw}}{C_{L\alpha,n} + C_{L\alpha,wb} + C_{L\alpha,bw}}$$

Where the lift curve slope accounting for each interference effect is found from the interference parameters.[20]

$$C_{L\alpha,wb} = K_{WB} C_{L\alpha,wg}$$
$$C_{L\alpha,bw} = K_{BW} C_{L\alpha,wg}$$
$$C_{L\alpha,n} = C_{L\alpha,b} \frac{\pi d^2}{4S_w}$$

The effect of lift carryover from the body onto the wing does not shift the wing aerodynamic centre considerably and so the following assumption can be made.[20]

$$\left(\frac{x_{ac}}{c_r}\right)_{wb} = \left(\frac{x_{ac}}{c_r}\right)_{wg}$$

A wing is considered to have a low aspect ratio under the following conditions:[20]

Subsonic: $AR\sqrt{1 - M^2} > 4$

Supersonic: $AR\sqrt{M^2 - 1}(1 + \lambda)\left(1 + \frac{1}{cot(\chi_{LE})\sqrt{M^2 - 1}}\right) > 4$

For high aspect ratio wings the lift carryover from the wing onto the body affects the vehicle aerodynamic centre as follows in the subsonic regime and from experimental data in the supersonic regime, where $k = \frac{d}{b}$.

$$\left(\frac{x_{ac}}{c_r}\right)_{bw} = \frac{1}{4} + \frac{b - d}{2c_r} \tan \chi_{\frac{c}{4}} \left(-\frac{k}{1 - k} + \frac{\sqrt{1 - 2k}\ln\left(\frac{1-k}{k} + \frac{1}{k}\sqrt{1-2k}\right) - (1-k) + \frac{\pi}{2}k}{\frac{k(1-k)}{\sqrt{1-2k}}\ln\left(\frac{1-k}{k} + \frac{1}{k}\sqrt{1-2k}\right) + \frac{(1-k)^2}{k} - \frac{\pi}{2}(1-k)}\right)$$

For low aspect ratio wings experimental data is used and then interpolated against the high aspect ratio case.

The effect of nose upwash on vehicle aerodynamic centre is found from experimental data depending on the nose type.
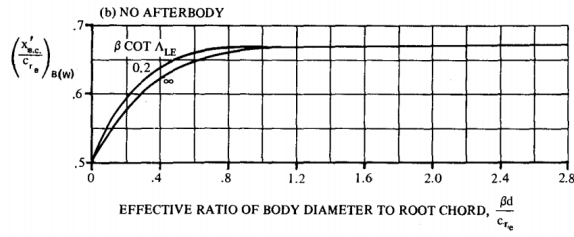
Figure 4.17: Xbw for supersonic high aspect ratio wings.[20]
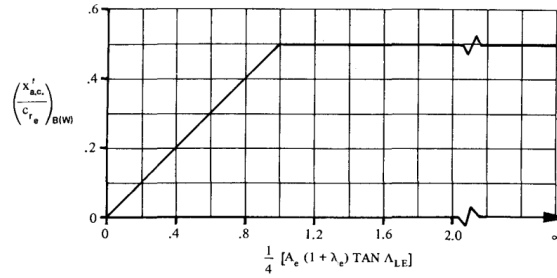
Figure 4.18: Xbw for low aspect ratio wings.[20]
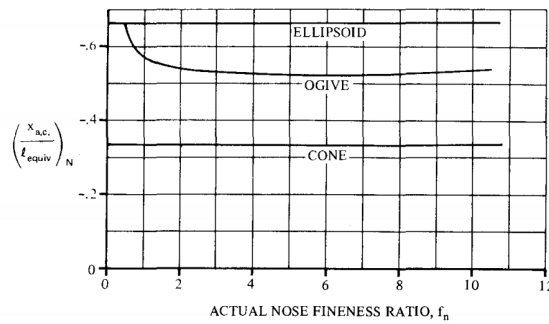
Figure 4.19: Subsonic nose centre of pressure location.[20]

4.4 Control surfaces

For the longitudinal dynamics, the role of elevators in extending the lift (and hence lift slope C_{L_α}) of a wing surface must be considered. This additional lift will also shift the location of the wing aerodynamic centre and will affect the degree of induced drag. The nature of control surface effectiveness depends on the speed regime in which the vehicle is flying.

The effect on lift will depend on the type and shape of flap as well as the degree that it is extended. It is assumed for the sake of simplicity that all vehicle flaps will be symmetrical, plain, trailing edge flaps. They will be deflected only between 0° and 15°. The hinge moment need not be considered, as it is assumed that the all vehicles are designed to have enough power to
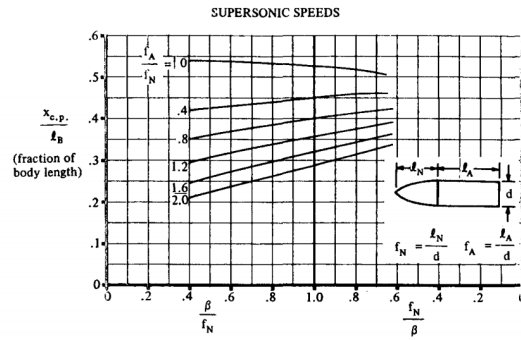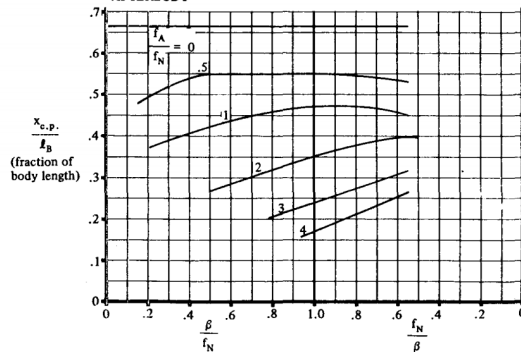
Figure 4.20: Supersonic nose centre of pressure location.[20]

deflect the fins in all flight regimes.

The contribution to the total body lift and moment due to the flaps will be elaborated for the subsonic and supersonic regime. In the transonic regime, an interpolation will occur between the subsonic and supersonic results. In the hypersonic regime the flaps will be assumed to operate the same as in the supersonic regime due to a lack of appropriate data.

Subsonic lift. A semi-empirical equation can be used to obtain the section based wing lift coefficient based on the flap lift effectiveness and several correction factors. [20]

$$c_{l_\delta} = \delta_f \left(\frac{c_{l_\delta}}{c_{l_{\delta,theory}}} \right) c_{l_{\delta,theory}} K'$$

- $c_{l_{\delta,theory}}$ is the theoretical flap effectiveness.

- $\dfrac{c_{l_\delta}}{c_{l_{\delta,theory}}}$ is an empirical correction factor.

- K' is a correction factor for non-linear effects at high deflections.

33
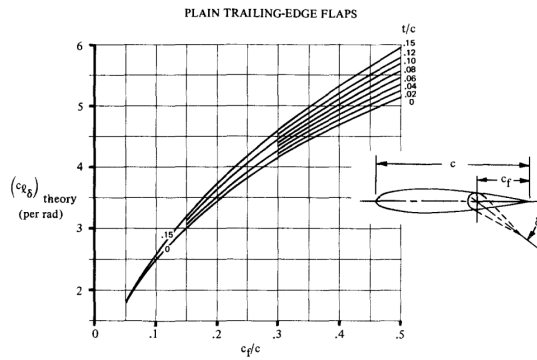
Figure 4.21: Flap lift effectiveness[20]
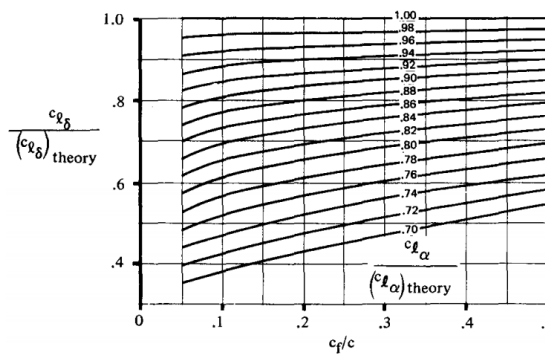
Figure 4.22: Empirical flap section correction factor.[20]
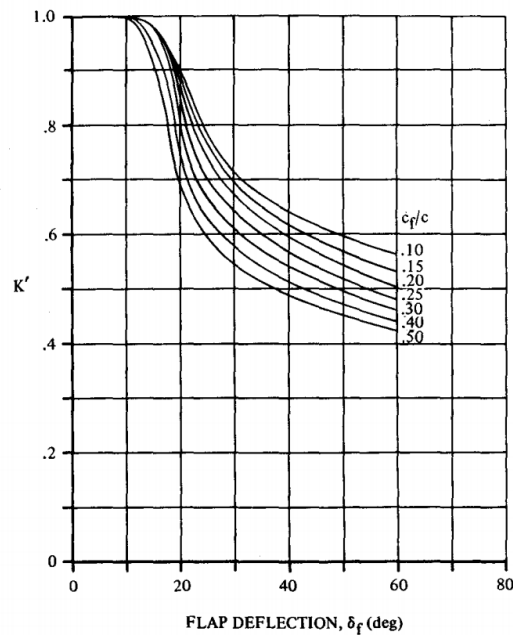
Figure 4.23: High deflection flap section correction factor[20]

34

The section lift effectiveness can be converted to the wing lift effectiveness by considering 3D wing effects.

$$\Delta C_L = \Delta c_{l_\delta} \left(\frac{C_{L_{\alpha,wg}}}{c_{l_{\alpha,wg}}} \right) \left(\frac{(\alpha_\delta)_{C_L}}{(\alpha_\delta)_{c_l}} \right) K_b$$

- $C_{L_{\alpha,wg}}$ is the wing lift curve slope

- $c_{l_{\alpha,wg}}$ is the section lift curve slope

- $\left(\frac{(\alpha_\delta)_{C_L}}{(\alpha_\delta)_{c_l}} \right)$ is a correction factor accounting for a finite wing span.

- K_b is a correction factor accounting for flap span location.
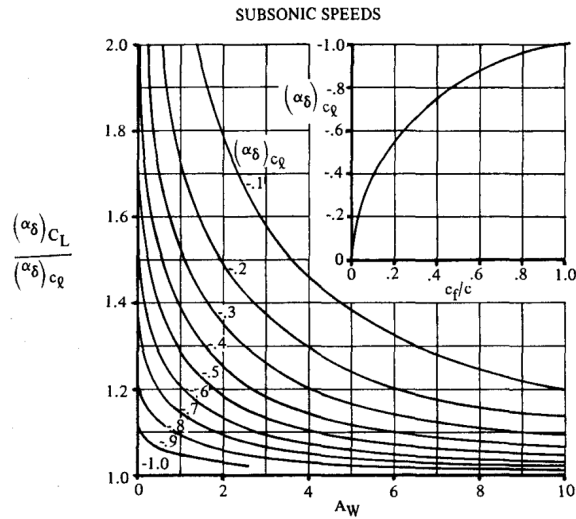
Figure 4.24: Correction factor accounting for wing finite span.[20]

Subsonic moment. The subsonic flap moment contribution is found from the following:[20]

$$C_{m_{CG,F}} = K_p \frac{\Delta Cm}{\Delta C_L} C_{L_F} + K_\chi \frac{AR}{1.5} C_{L_F} \tan(\chi_{25})$$

- K_p is a correction factor for wing taper and flap inboard location.

- K_χ is a correction factor for wing sweep.

- $\frac{\Delta Cm}{\Delta C_L}$ is the ratio of lift force increment to moment increment.

35
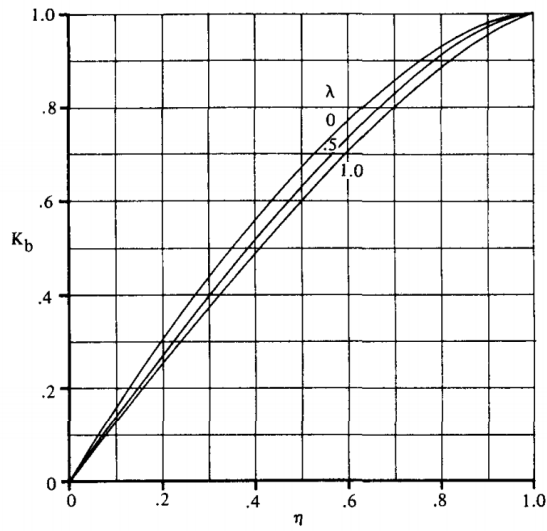
Figure 4.25: Correction factor accounting for flap inboard and outboard span location, (η).[20]
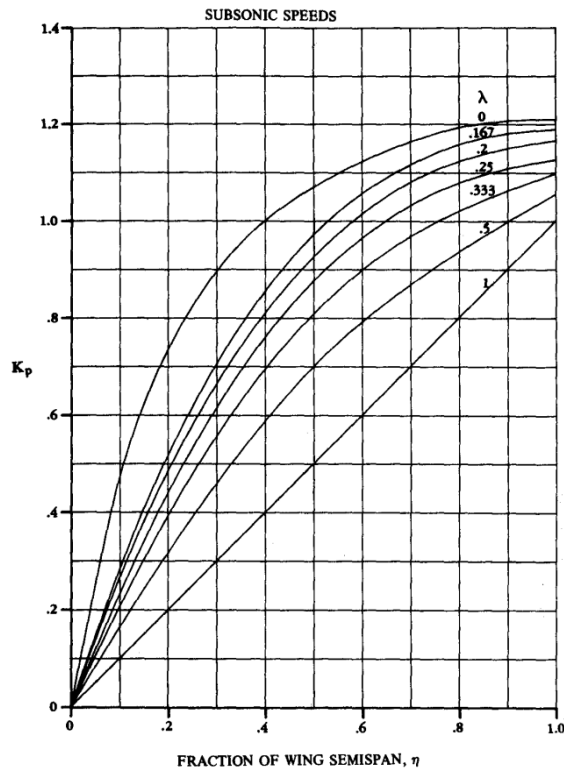
Figure 4.26: Flap moment correction factor accounting for taper and wing span location[20]

Supersonic lift. The supersonic lift can be found by considering the Busemann coefficients C_1, C_2 and the angle of the wing trailing edge ϕ_{TE}.[20]
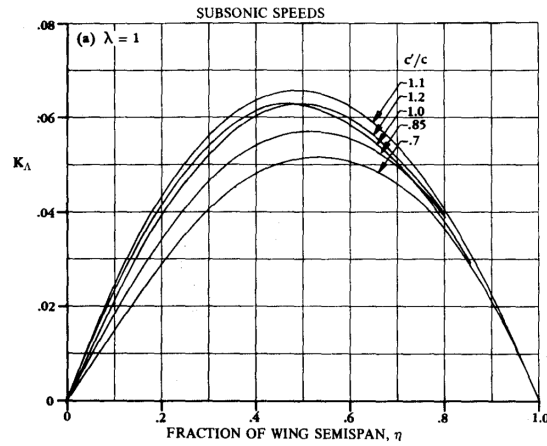
Figure 4.27: Flap moment correction factor accounting for sweep.[20]
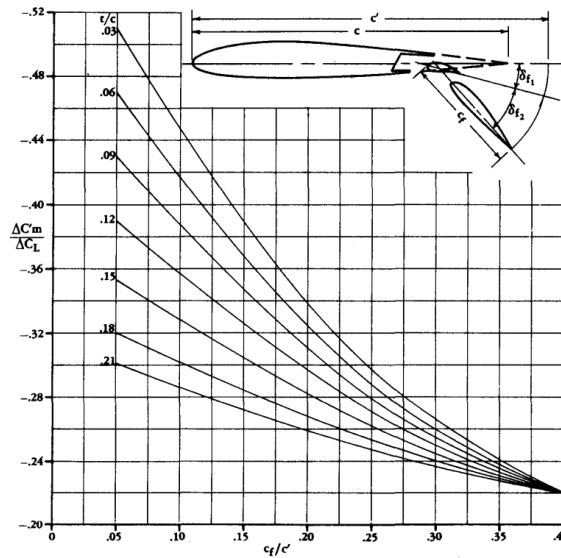
Figure 4.28: Flap moment increment to lift increment ratio.[20]

$$\Delta C_L = \left(1 - \frac{C_2}{C_1}\phi_{TE}\right) C'_{L_\delta} \frac{S_f}{S_w}$$

$$C_1 = \frac{2}{\sqrt{M^2-1}}$$
$$C_2 = \frac{(\gamma+1)M^4-4(M^2-1)}{2(M^2-1)^2}$$

The uncorrected supersonic lift effectiveness is found from experimental data.

Supersonic moment. The supersonic moment can be found in a similar fashion to the lift as the Busemann coefficients are likewise significant.[20]

$$K_1 = \left(1 - \frac{C_2}{C_1}\phi_{TE}\right) (3)$$

37
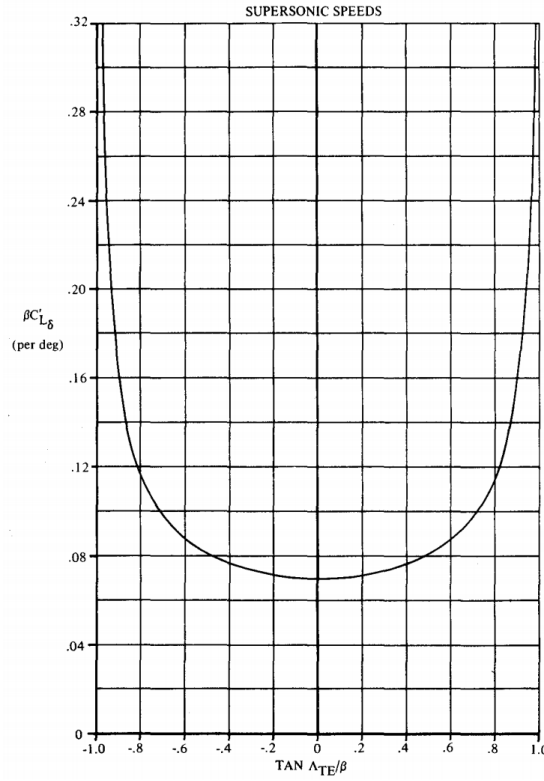
Figure 4.29: Supersonic lift effectiveness.[20]

$$K_2 = \left(1 - \frac{C_2}{C_1}\phi_{TE}\right)(\tan\chi_{TE})$$
$$K_3 = \left(1 - \frac{C_2}{C_1}\phi_{TE}\right)$$

$$C_{m_\delta} = K_1 \frac{1}{3} \frac{b_f}{c_{MAC}} \frac{c_f}{S_w} C_{m_{\delta,0}} - K_1 \frac{1}{2} \frac{b_f}{c_{MAC}} \frac{c_f}{S_w} C_{roll_\delta} - K_3 \frac{X_f}{c_{MAC}} \frac{S_f}{S_w} C_{L_\delta}$$

- $C_{m_{\delta,0}}$ is the flap pitching moment effectiveness

- C_{L_δ} is the flap lift effectiveness, as calculated in the supersonic lift section

- C_{roll_δ} is the flap roll effectiveness

The flap roll effectiveness is calculated from a semi-empirical relationship, which in turn is a function of the uncorrected flap roll effectiveness, $C_{roll_{\delta,0}}$, that is found from experimental data.

$$C_{roll_\delta} = \left(1 - \frac{C_2}{C_1}\phi_{TE}\right) C_{L_\delta} \frac{S_f}{S_w} \frac{1}{2} \frac{\eta_i}{b_w} + \frac{b_f}{2b_w} \frac{C_{roll_{\delta,0}}}{C_{L_\delta}}$$

38
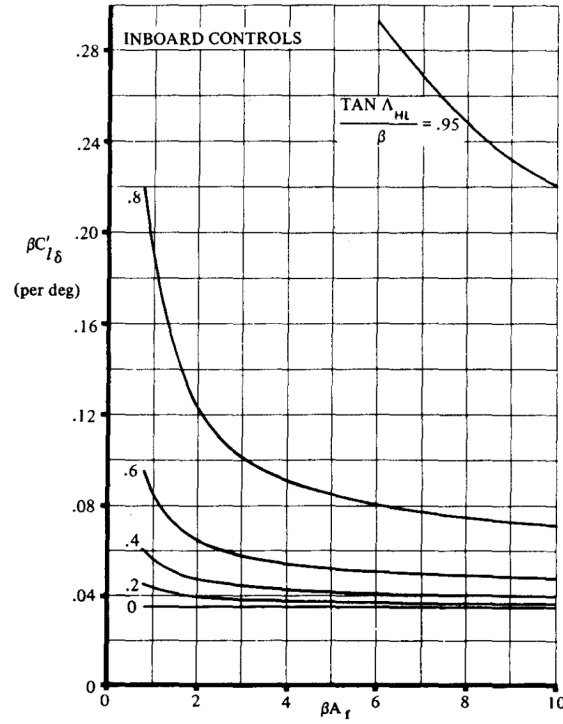
Figure 4.30: Supersonic roll effectiveness.[20]

▌ 4.5 High angle of attack aerodynamics

When considering the vehicle at high angles of attack, the small angle approximation used to justify the linear theory for the lift and moment is no longer valid. Additionally, the wing will experience stall and viscous flow separation changing the nature of the drag to being more like a flat plate against crossflow.

The body lift, drag, and moment are as presented for the low angle of attack, but with a trigonometric relationship instead to account for the breakdown in the low angle approximation. This also scales the aerodynamic force to account for the behaviour as the body becomes more perpendicular to the flow and lift approaches zero.[34]

$$C_{L_B} = (k_2 - k_1)\frac{S_b}{S_{ref}}\sin 2\alpha \cos\frac{\alpha}{2} + \eta C_{D_c}\frac{S_p}{S_{ref}}\sin^2\alpha - C_{D_{B,0}}\cos^2\alpha\sin\alpha$$

$$C_{m_{B,CG}} = (k_2 - k_1)\frac{V - S_b(l - x_{cg})}{S_{ref}l_{ref}}\sin 2\alpha \cos\frac{\alpha}{2} + \eta C_{D_c}\frac{S_p}{S_{ref}}\frac{x_{cg} - x_p}{l_{ref}}\sin^2\alpha$$

$$C_{D_B} = (k_2 - k_1)\frac{S_b}{S_{ref}}\sin^2\alpha + \eta C_{D_c}\frac{S_p}{S_{ref}}\sin^3\alpha$$

The non-linear lift is modelled as a flat plate and scales the cross flow coefficient

39

of lift and drag with the angle of attack. Additionally, there are contributions to lift from the wing-body interaction and deflections of the flap.[34]

$$C_{LW} = C_{D_{c,W}} \frac{S_w}{S_{ref}} \sin^2 \alpha \cos \alpha$$

$$C_{L_{\alpha,WB}} = K_{WB} \frac{S_w}{S_b} C_{L_\alpha} \sin \alpha \cos \alpha$$
$$C_{L_{\alpha,BW}} = K_{BW} \frac{S_w}{S_b} C_{L_\alpha} \sin \alpha \cos \alpha$$
$$C_{L_{\delta,WB}} = K_{WB'} \frac{S_w}{S_b} C_{L_\alpha} \sin \delta \cos(\alpha + \delta)$$
$$C_{L_{\delta,BW}} = K_{BW'} \frac{S_w}{S_b} C_{L_\alpha} \sin \delta \cos(\alpha + \delta)$$

For the viscous separation effect on drag force, the wing is treated as a flat plate tilting in cross flow.[34]

$$C_{DW} = C_{D_{fp}} \frac{S_w}{S_{ref}} \sin \alpha$$

The total lift and drag force on the body can therefore be calculated.

$$C_{LV} = C_{LW} + C_{LB} + C_{L_{\alpha,WB}} + C_{L_{\alpha,BW}} + C_{L_{\delta,WB}} + C_{L_{\delta,BW}}$$
$$C_{DV} = C_{DW} + C_{DB}$$
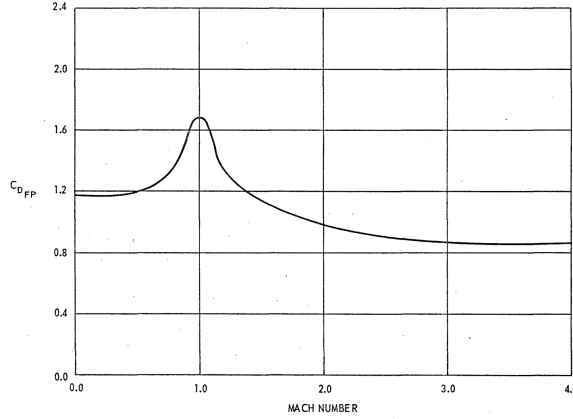
Figure 4.31: Wing drag coefficient when acting as a flat plate, $C_{D_{fp}}$ [34]

The pitching moment and the centre of pressure of the wing are found from the contribution of wing lift and drag forces and wing-body interaction effects. The location of the wing centre of pressure due to interaction effects, $X_{cp,WB}$ and $X_{cp,BW}$ are found from experimental data.[34]

$$C_{mW} = ((C_{L_{\alpha,WB}} + C_{LW}) \cos \alpha + C_{DW} \sin \alpha)(\frac{X_{cp,WB}}{l_b}) + (C_{L_{\alpha,WB}} \cos \alpha + C_{L_{\delta,BW}})\frac{X_{cp_{BW}}}{l_b}$$

$$X_{cp,W} = \frac{C_{mW} l_b}{(C_{L_{\alpha,WB}} + C_{L_{\alpha,BW}} + C_{LW}) \cos \alpha + (C_{L_{\delta,WB}} + C_{L_{\delta,BW}} + C_{DW}) \sin \alpha}$$

The vehicle moment is the sum of the contribution from each part.

$$C_{m_{CG}} = C_{m_B} + C_{m_W} \frac{X_{cg} - X_{cp,W}}{X_{cp,W}}$$

Chapter **5**

Curve fitting aerodynamic data

The theory from Chapter 4 has been compiled and programmed into a MATLAB code, alongside the relevant data sets used in calculation of the aerodynamic properties, and vehicle parameters. This code is then used to calculate the total lift, drag, and moment coefficients of a vehicle depending upon its geometric parameters, and for a user defined range of Mach numbers and angles of attack.

The Mach range to be considered is from zero to ten, to encapsulate the behaviour in all speed regimes. Beyond this Mach number the vehicle has converged towards the hypersonic limit for its aerodynamic coefficients, and further increases in speed negligibly affect these properties. The Mach resolution of the data grid [0:0.05:1.5], to encapsulate higher precision in the transonic regime where the data is more sensitive to changes in Mach number, then [2:0.5:6] for the supersonic and [7:1:10] for the hypersonic regime.

The range of angle of attack will be from -90° to 90°, representing the vehicle tilting entirely upwards and entirely downwards. Allowing the vehicle to enter these very high angles of attack is certainly necessary, for the vehicle to be able to perform its final thrust boost opposite the direction of motion to bring the terminal velocity down to an acceptable landing value. A resolution of one degree between points is used to generate the data.

With this data, aerodynamic coefficient is represented with a function of only two variables, Mach number and angle of attack.

$$C_L, C_D, C_M = f(\alpha, M)$$

The aerodynamic coefficients varies with angle of attack in a sinusoidal fashion, due to the theoretical contribution from Allen and Perkins crossflow theory. The drag coefficient has a period of 2π, and the lift and moment coefficients of π. This is an intuitive result, as a streamlined aerodynamic body parallel

to crossflow should experience very low drag compared to that same vehicle perpendicular to crossflow, where much more of its surface will be buffeted by wind. When the vehicle is directly parallel or perpendicular to the crossflow, the vehicle will not experience (non-negligible) lift, due to the symmetry of the body. It is important to note that this is largely due to the fact that the airfoils selected are also symmetric, if they had a camber there would indeed be lift at zero angle of attack. The moment data is similarly characterised as being close to zero at 0° and $\pm90^o$ and maximised near 5° and minimised near -5°.

Along the Mach number axis, the data is characterised by peaks in the transonic regime. This transonic peak, arising due to high wave drag as well as skin friction drag, is a common aerodynamic feature and has been found many times in experimental data.

The most obvious discontinuity in this data is the jump from the low angle of attack region to the high angle of attack region. This is because two significantly different treatments of the aerodynamic properties are used in both, with the low angle of attack methods significantly underestimating the high angle of attack properties and the high angle of attack data methods overestimating the data.

Indeed, the discontinuity for the moment coefficient is particularly prominent, with different trends occurring in both regions. This is due to the nature of aerodynamic stall. In the low angle of attack region the contribution due to the wing is to act like a conventional airfoil. The neutral point is aft of the centre of gravity, resulting in static stability whereby increasing the angle of attack results in a negative restoring moment and vice versa. In the high angle of attack range, however, the flow over the airfoil is disturbed by stall and flow separation, and so the wing acts more like a plate. Additionally, more of the mass of the body contributes to the total vehicle moment as it lifts up and experiences crossflow. Increasing the angle of attack in this case results in a greater moment, as the vehicle neutral point has moved to an unstable location. This explains the discrepancy in the moment data.
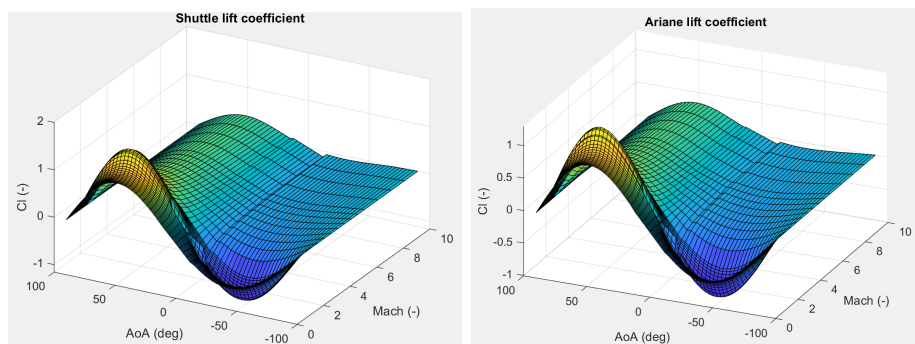
Data must also be modelled to account for how the vehicle's aerodynamic properties change with the deflection of the control surface. To account for
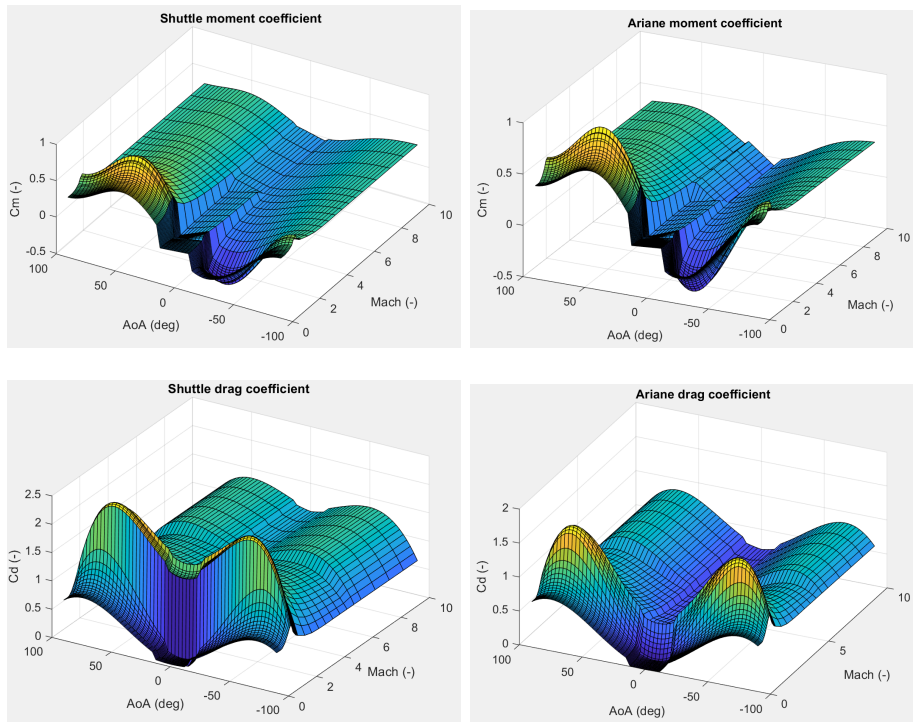
Figure 5.1: Drag, lift and moment coefficients for the Ariane V LFBB and Shuttle Orbiter

this, it will be assumed that there is a linear relationship between the change in coefficient due to the control surface and the control surface deflection angle. In this sense, by calculating the control derivatives for the aerodynamic coefficients, and multiplying those values by the magnitude of deflection, the total contribution of the control surface can be found. The same grid of α and Mach values is used in finding these derivatives.

$$C_L = C_{L_0} + \delta C_{L_\delta}$$
$$C_m = C_{m_0} + \delta C_{m_\delta}$$

5.1 Curve fitting

As the aerodynamic data is highly discontinuous, especially when transitioning from one flight regime to another, this poses problems with simulating and optimising the differential equations of motion. Runge-Kutta solvers in MATLAB, as they use the Euler method and hence function derivatives for numerically solving and projecting forward states of the differential equation set. Likewise problems can arise when attempting to optimise a non-smooth problem with the MATLAB solver FMINCON.
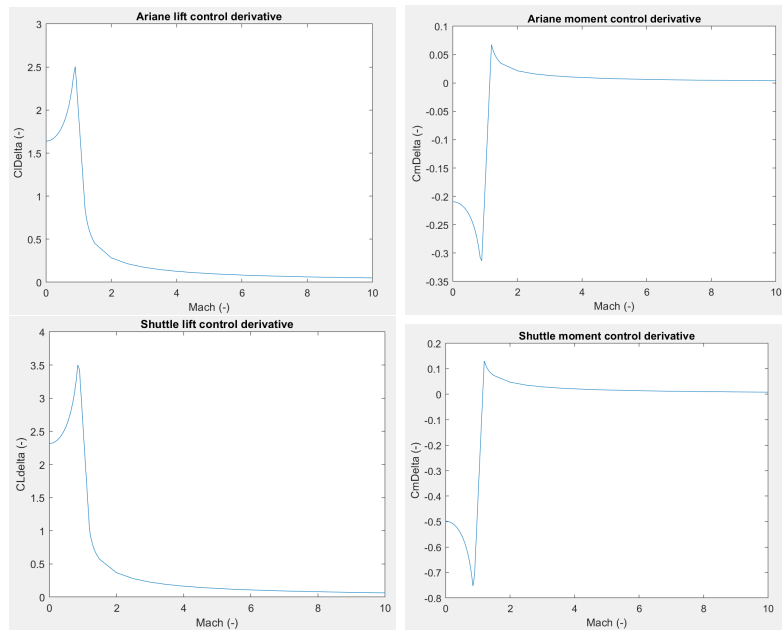
Figure 5.2: Lift and moment control derivatives for the Ariane V LFBB and Shuttle Orbiter

In order to avoid these problems, a continuous and smooth surface function will be calculated with the aerodynamic data for both vehicles. TableCurve 3D from SYSTAT Software will be used to generate this function, as the software can automatically fit over 3000 function types over data and rank them in order of a goodness of fit value.[1] This process was carried out for both vehicles, and the functions used for the five aerodynamic coefficients for each vehicle can be contrasted with the original data.
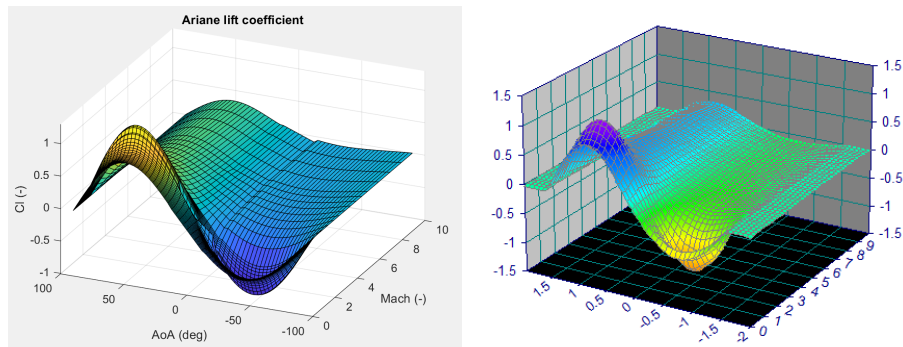
The equations used to fit the data consist variously of Chebyshev rational order polynomials and Sigmoid, Fourier, and cosine series bivariates. The description of these functions, as well as the fitted coefficients, are provided in Appendix 1.

The fits capture many of the important aerodynamic features of the two vehicles, including the peaks in the transonic region and the general relationship

46
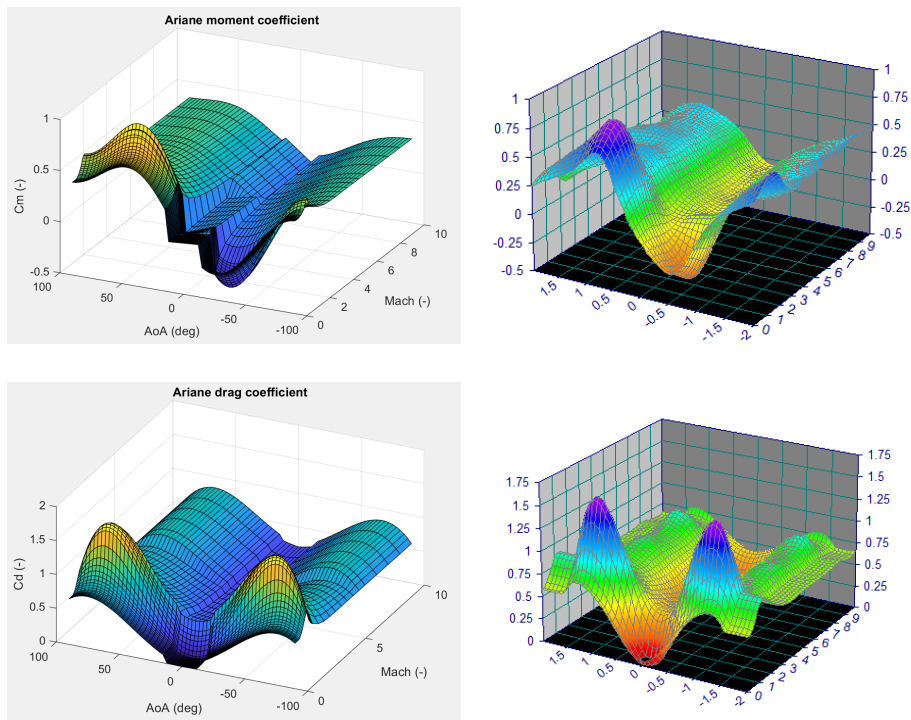
Figure 5.3: Ariane coefficient data (left) compared to approximate fits (right)
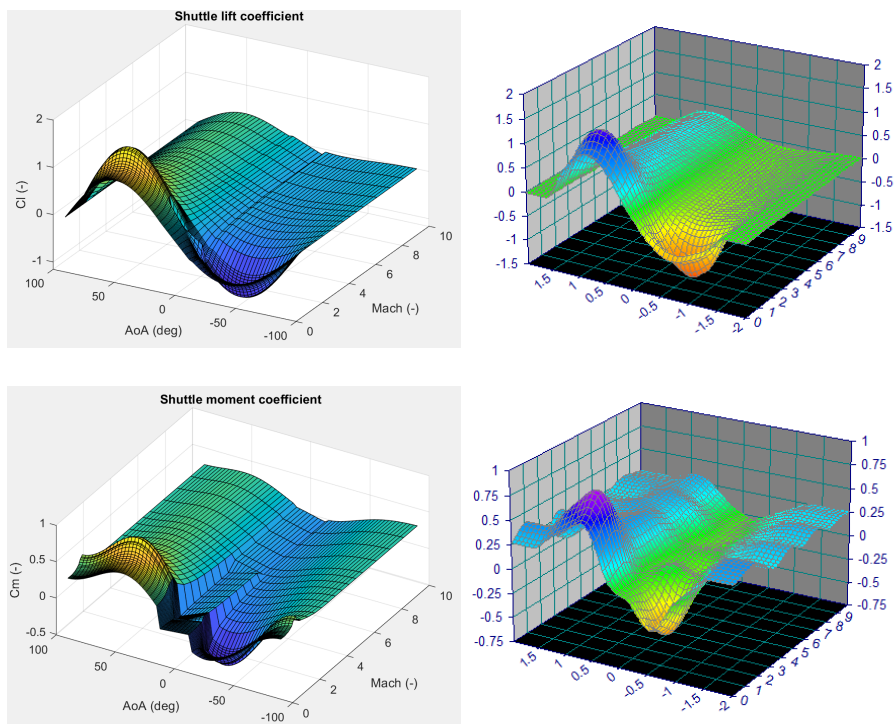
with angle of attack. Less accurately captured are regions characterised by sudden changes in behaviour, such as the introduction of stall at moderate angles of attack, and the breakdown of attached flow theory in the hypersonic
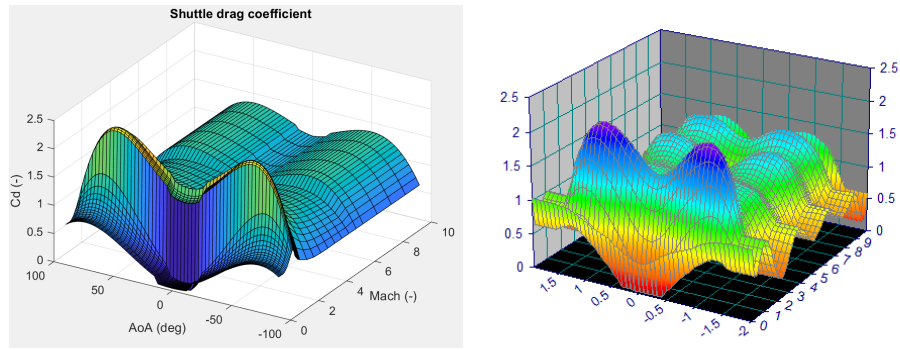
Figure 5.4: Shuttle coefficient data (left) compared to approximate fits (right)

region. The validity of the fit compared to the supplied data can be numerically estimated through a coefficient of determination r^2, where a value closer to 1 is a better correlation. This parameter depends on the sum of residuals squared SSE, which is a measure of the difference between the estimated and actual data point, as well as the sum of squares about the mean, SSM, which compares the estimated data to the mean value of the actual data. The fitted equations have good correlation, with $r^2 > 0.95$ for all data except for the Shuttle drag coefficient, where $r^2 = 0.85$.

$$r^2 = 1 - \frac{SSE}{SSM}$$

Another important correction that must be made is to scale the equations for drag to ensure that no local minimum yields a negative coefficient, a physically nonsensical result that is introduced due to the imperfect modelling of the fits.

It is also important to note that for especially high order polynomials, the curve fit is often only as good as the range of data it was fitted on.[1] Moving increasingly far away from the range of data, in this case a Mach number from 0 to 10 and an angle of attack from -90° to 90° can result in wildly divergent behaviour. To avoid this, bounds will be imposed on the constraints in simulations and optimisation to ensure that the functions are not required to calculate outside of the appropriate range for use. Also high order fits tend to result in the generation of many local maxima and minima as it tries to fit the global trends of the data better. This is particularly apparent for the curve fits for the Shuttle drag and moment. This can be a problem for optimization solvers that may become stuck within the region of one of these local minima, further emphasising the importance of providing a good initial guess for this problem in particular.

Chapter 6

Flight simulation

6.1 Simulation results

Now that the aerodynamic functions, vehicle properties, and surrounding environment have been described, the states can be propagated forward according to the fully described equations of motion to see how the modelled vehicle actually behaves dynamically when experiencing re-entry.

To simulate the model, MATLAB's ODE45 function will be used. ODE45 is a problem solver suited to solving initial value differential equations of form $y' = f(y, t)$, which is suitable for the re-entry differential equations. The solver works by using the classical Runge-Kutta algorithm, using variable step sizes that are selected to improve the speed of program execution. It is also possible to incorporate events into the solver, such as when states or the time variable take on a particular value. In this case, the solver has been programmed to terminate once the altitude state reaches zero.

Using this solver, some test scenarios can be performed using the equations of motion. For the first case, purely gravitational force can be considered by treating the aerodynamic coefficients as being zero. Modeling a circular orbit case, elliptical orbit case, as well as a suborbital parabolic trajectory will confirm that the equations of motion are behaving as expected. For these tests, the Ariane V LFBB model will be considered at full mass and uncontrolled flight.

Circular orbit. For a circular orbit, the vehicle should be travelling always tangential to the Earth's radial vector, with a constant velocity and altitude. The orbital plane of motion is arbitrary, however the vehicle should complete a full rotation in the plane indicated by the true anomaly which should vary periodically from 0 to 2π.

At an altitude of h = 400km, the speed required to maintain a circular orbit is

$$V = \sqrt{\frac{\mu_E}{r_E + h}} = \sqrt{\frac{3.963 \times 10^{14}}{6.357 \times 10^6 + 400000}} = 7658 \frac{m}{s}$$

By considering and then plotting the states in the orbital plane as $[(h + r_E)\sin(\theta), (h + r_E)\cos(\theta)]$ the trajectory of the vehicle in the plane can be plotted. The result is circular motion as is expected, with velocity and flight path angle constant.
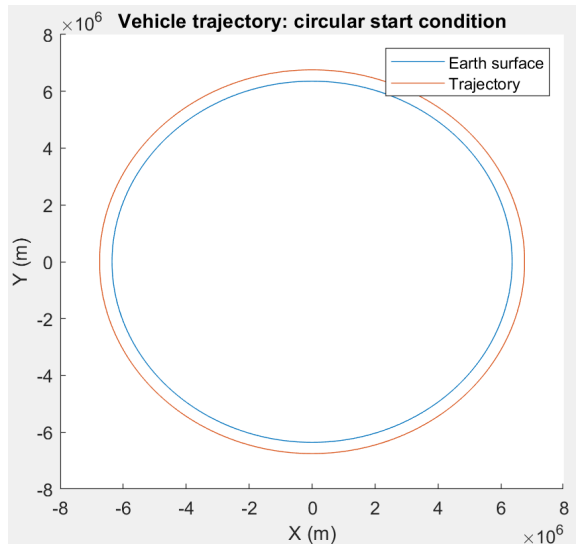
Figure 6.1: Trajectory for circular orbit starting condition

Elliptical orbit. An elliptical orbit can be defined with an perigee altitude of 10km and an apogee twice the Earth's radius. To reach this apogee, the perigee velocity must be $9107\frac{m}{s}$ with a flight path angle of 0°. We can further test the re-entry equations of motion by integrating these states forward for this scenario. Figure 6.2 demonstrates that the trajectory is in fact circular, however the apogee altitude is 10km lower than expected, a small number when dealing with distances of multiple Earth radii and likely due to imprecision in the solver and the output time step.

Re-entry simulations. There are several typical flight profiles depending on the vehicle and the nature of the mission. For Falcon 9 flights, the first stage can land far downrange of the launch site by continuing on its suborbital parabolic trajectory after separation, followed by a reverse boost to reduce speed. It can also land near to the launch site by performing a boost-back burn, changing the trajectory of the vehicle from its original suborbital trajectory to a new one directed back towards the site.
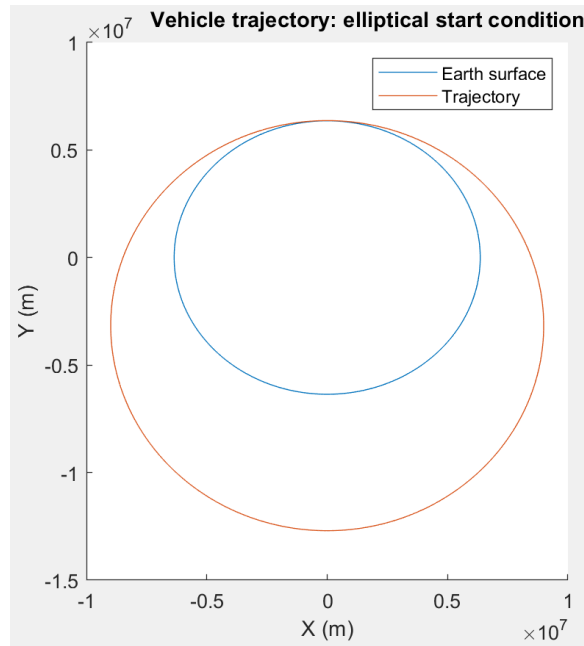
Figure 6.2: Trajectory for elliptical orbit starting condition
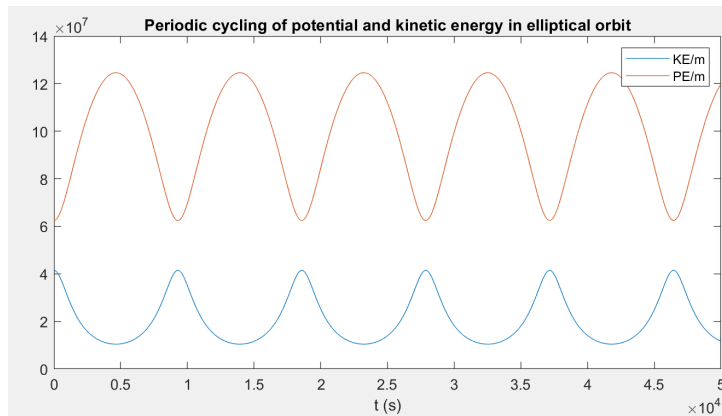
Figure 6.3: Cycling nature of potential and kinetic energy

This first case will be considered for testing a re-entry scenario for the Ariane V LFBB. Specifically, the conditions for the flight profile will be based on the Starlink v1.0 L4 flight of the Falcon 9, with estimations of its flight state provided by the online simulation software Space Club. At 390s into the mission, the vehicle re-enters the atmosphere at 80km, with a velocity of $2150\frac{m}{s}$ and flight path angle of -27°. As this vehicle is moving very quickly and with a large mass, it will experience the atmosphere essentially as a discontinuity. Aerodynamic forces will be comparatively negligible. Instead, a shallower flight path angle of 1° will be considered, so that the vehicle spends more time in the denser parts of the atmosphere where the aerodynamics will have more effect. This will serve as the initial condition for the state propagator and will be used to test the aerodynamic loads experienced by

51
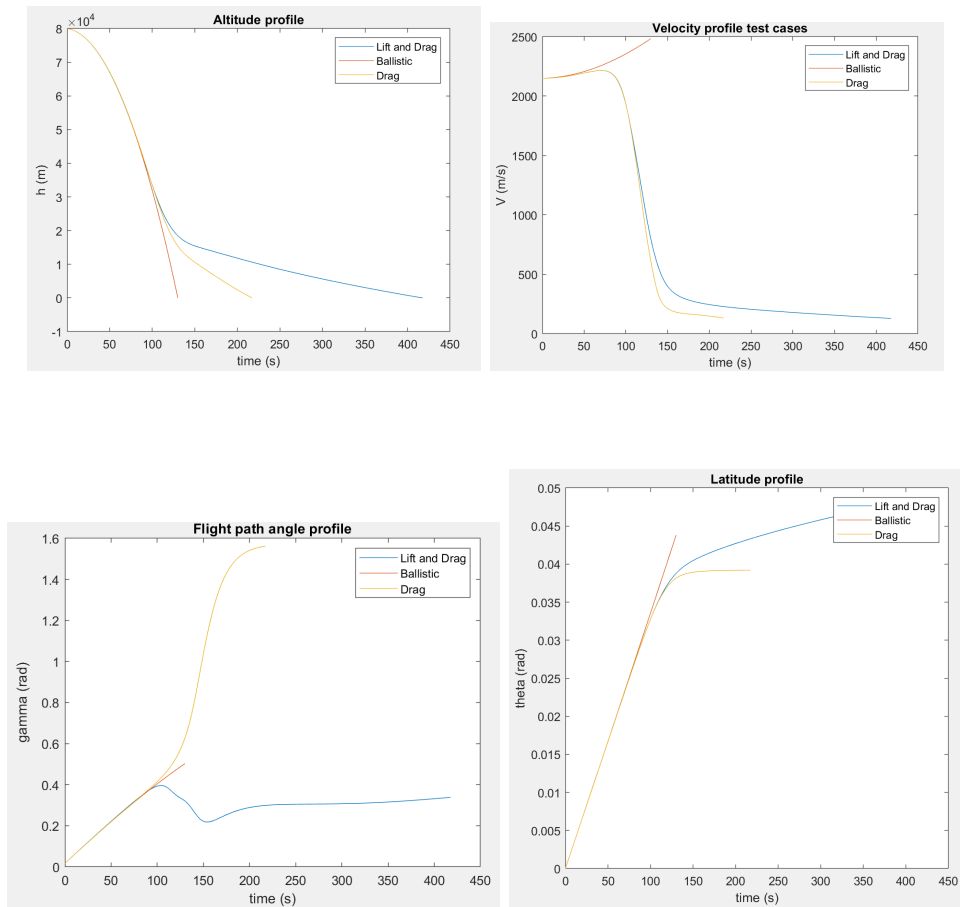
the vehicle.

Figure 6.4: Profile for ballistic, drag only, and lifting re-entries

As can be seen from figure 6.4, the vehicle aerodynamics are behaving in an intuitive sense. When drag is present, the vehicle loses speed as it descends through the atmosphere instead of gaining speed. Eventually it reaches a terminal velocity at around 150s, although this terminal velocity continues to change slightly as the atmospheric density decreases and the aerodynamic coefficients vary. This terminal velocity seems also to be of a reasonable order of magnitude.

The effect of lift is to further increase the time of flight and downrange distance, with a much more pronounced effect than the increase from the drag alone case. Critically, the flight path angle expresses markedly different behaviour. The vehicle experiences a gliding descent with a shallow re-entry angle of about 17°, unlike the drag only case where the reduction in forward speed means the vehicle is the downwards acceleration of gravity becomes relatively more noticeable, until the vehicle is eventually falling directly downwards.

6.2 Comparison with HyperSMS

Re-entry simulation software exists in the form of HyperSMS, which is more involved with the effects of communication blackout and thermal loads in hypersonic, high-altitude flight but which does include a rudimentary trajectory propagator.[14] In this toolbox, the same equations of motion are used however the calculation of the aerodynamic properties varies, with less emphasis on the effect of the vehicle features and more emphasis on the effect of the hypersonic ionized flow.

By comparing the starting condition of $700\frac{m}{s}$ at a 1° flight angle and 80km altitude, the aerodynamic model used in this report can be validated. Again, the vehicle properties of the Ariane V LFBB are to be used.
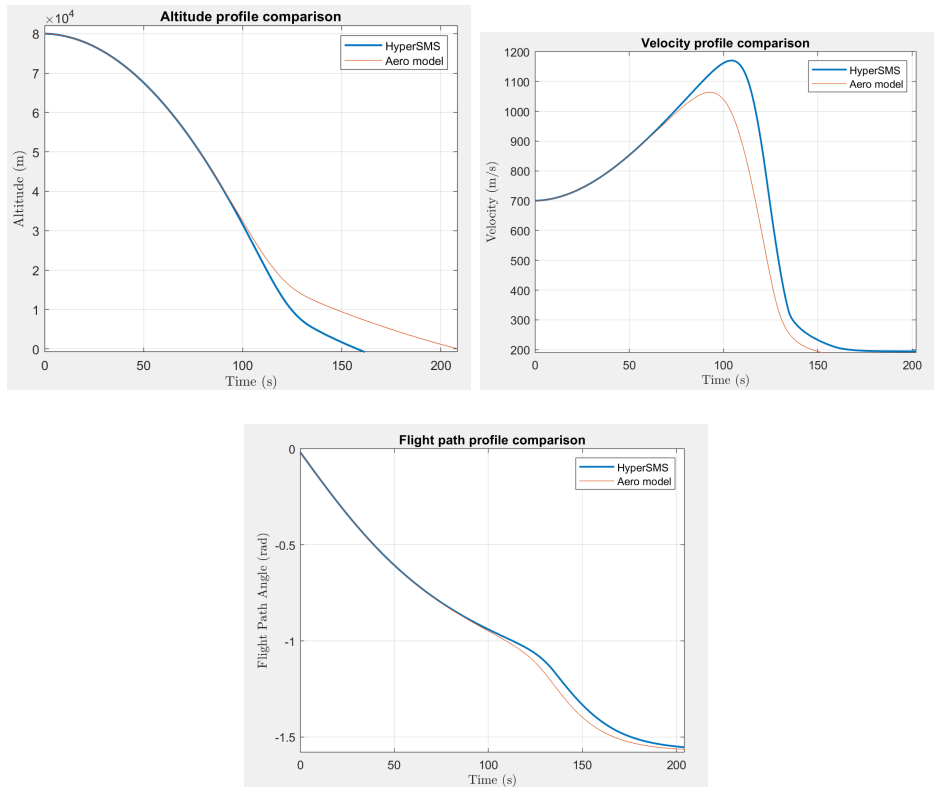
Figure 6.5: Comparison of flight profile for aerodynamic model with HyperSMS model.

The aerodynamic model used in this investigation shows good agreement with that used in the HyperSMS simulation package. It is worth noting that the time of flight is greater when compared to the same conditions for HyperSMS and the velocity lower. This means that the drag and lift coefficients are estimated as being higher compared to the HyperSMS model. While this may be a modelling error that merits further investigation, by modelling the effect of angle of attack and the wing shape, higher lift coefficients should occur.

Chapter 7

Trajectory optimization

The central question of this investigation is whether a system under arbitrary but bounded control can be moved successfully from one starting state to a desired end state, which characterises an acceptable 'landing' condition. The set of starting states that can accomplish this is the space of the flight envelope, which we seek to find. This can be framed as an optimal control problem. Although there are possibly many pathways to get to the end state, one could seek to minimise the control response, time of flight, aerodynamic load, or any other such factor to further constrain the system.

7.1 Optimal control

Optimal control involves using the principles of calculus to find local minima or maxima for a function $J = f(x)$. Typically this function is constrained by the relationship $\dot{x} = f(x, u, t)$, which describes the dynamics of the system, and a control vector u is found that minimises $J = f(u)$ subject to this.

Re-entry trajectory dynamics are non-linear in nature and as such a solution methodology suitable for non-linear optimal control problems must be considered. The non-linear optimal control problem is posed in Bolza form as follows, where M is the Mayer term which quantifies the terminal cost and L is the Lagrange term that quantifies the running cost.

$$min_u J(x, u, t_0, t_f) = M(x(t_0), x(t_f), t_0, t_f) + \int_{t_0}^{t_f} L(x(t), u(t), t)dt$$

Subject to:

$$\dot{x} = f(x, u, t)$$
$$C(x, u, t) \leq 0$$
$$\phi(t_0, x(t_0), t_f, x(t_f)) \leq 0$$

7.2   Solution methodology

The two main methods used to solve optimal control problems are the direct and indirect methods. Indirect methods solve the necessary conditions of optimality using calculus of variations. Direct methods discretize the problem and then computationally iterate towards the minimum point. Direct solutions are of course more approximate as the accuracy is restricted to the domain that results from discretization. The more nodes used in the discretization, the more accurate the optimal solution will be but the greater the computational time. Direct methods, however, are more robust for initial guesses, are easier to implement for complicated and non-linear dynamics, and have better convergence properties. Although indirect methods have been used to solve trajectory optimization problems (more commonly in space and not for atmospheric re-entry, however), direct methods instead will be used.

Direct methods consist of shooting and collocation. In direct shooting methods, the cost is calculated as the states are integrated forwards from their starting position. For the more robust multiple shooting case, a trajectory is broken into many smaller intervals, with simulations beginning at the start point of each interval, eventually calculating paths in which the trajectories are able to line up.[28] Direct collocation however, involves fitting piecewise polynomial functions onto the solution trajectory, with considerations of the system dynamics and constraints occuring at the collocation points. Again, a defect representing the difference between the actual trajectory and the fitted trajectory can be parameterized. Controls are then selected so that the defect tends towards zero.[28]

An open source multiple interval pseudospectral solver for MATLAB has been published by Daniel R. Herber that makes use of these direct collocation methods with the possibility to use either Chebyshev or Lagrange polynomials.[19] This solver is set up so that once the constraint functions and Lagrange and Meyer functions have been described, the system is automatically discretized and fed into MATLAB's FMINCON solver, allowing for an easy implementation. The solver has been demonstrated to yield optimal solutions for test cases such as the Bryson-Denham double integrator optimal and the Brachistochrone problem.

7.3   Problem set up

The aim is to find an envelope of starting states, a particular speed, flight path angle, altitude, angular distance from a launch site, to see what combination of these variables will enable the vehicle to reach that launch site and land correctly. To simplify this problem, trajectories can be considered for a vehicle

entering the atmosphere at 80km and for a range of different velocities and flight path angles. As the desired landing point is on the Earth's surface, all trajectories from space must pass through this altitude state and it is non meaningful for the scenario of this problem to consider vehicles that begin "re-entry" below this altitude.

By considering the maximum and minimum downrange distances for a vehicle starting at 80km with a full range of possible re-entry velocities and flight path angles, we can find how far away a vehicle must be from a landing site to be able to land. The initial latitude and longitude of the vehicle is also made irrelevant, as the maximum and minimum possible traversable distance (ie, whether or not the vehicle is in range) will be the same regardless of starting position. This is predicated upon the assumption that the atmosphere and gravity vary spatially only with altitude. If a higher fidelity gravitational and atmospheric model were used, then this methodology would not necessarily apply.

■ 7.3.1 Trajectory constraints

Recall that the general non-linear control problem is defined as follows.

$$min_u J(x, u, t_0, t_f) = M(x(t_0), x(t_f), t_0, t_f) + \int_{t_0}^{t_f} L(x(t), u(t), t)dt$$

Subject to:

$$\dot{x} = f(x, u, t)$$
$$C(x, u, t) \leq 0$$
$$\phi(t_0, x(t_0), t_f, x(t_f)) \leq 0$$

$\dot{x} = f(x, u, t)$ is the dynamic constraint, and defined by the equations of motion.

$$\frac{dV}{dt} = -\frac{D}{m} + \frac{T}{m}\cos\alpha - g\sin\gamma$$

$$\frac{d\gamma}{dt} = \frac{L(\delta)}{Vm} + \frac{T}{Vm}\sin\alpha - \frac{g}{V}\cos\gamma + \frac{V\cos\gamma}{R_e+h}$$

$$\frac{dh}{dt} = -V\sin\gamma$$

$$\frac{d\theta}{dt} = \frac{V\cos\gamma}{R_e+h}$$

Where lift and pitching moment are a function of the control surface deflection inputs, $L(u), M(u)$.

As the vehicle consumes fuel to increase the thrust, the vehicle mass changes also and should additionally be modelled as a state. Additionally, the rotational motion of the vehicle should be modelled too.

For the Shuttle's unpowered descent, the control inputs are the deflections of the flaps (δ_1, δ_2) that affect the lift and moment coefficients respectively.

For the Ariane V LFBB, the fuel mass flow rate $(\dot{m})$ will be controlled as will angle of attack (directly) (α), and the deflection of the flap (δ) to change the lift coefficient.

The dynamic constraints can therefore be provided for both vehicles as follows.

Ariane LFBB dynamics expressed in terms of states and controls:

$$\dot{X}_1 = -\frac{D}{X_5} + \frac{T}{X_5}\cos U_2 - g\sin X_2$$
$$\dot{X}_2 = \frac{L}{X_1 X_5} + \frac{T}{X_1 X_5}\sin U_2 - \frac{g}{X_1}\cos X_2 + \frac{X_1 \cos X_2}{R_e + X_3}$$
$$\dot{X}_3 = -X_1 \sin X_2$$
$$\dot{X}_4 = \frac{X_1 \cos X_2}{R_e + X_3}$$
$$\dot{X}_5 = -U_1$$

$$T = U_1 I_{sp} g + (P_{ex} - P_{atm})S_b$$
$$D = \tfrac{1}{2}S_{ref}C_D\rho X_1^2$$
$$L = \tfrac{1}{2}S_{ref}C_L\rho X_1^2$$

$$C_L = C_{L_0} + C_{L_\delta}U_3$$

$$g = g_0 \frac{r_E}{(r_E + X_3)^2}$$
$$\rho = \rho_0 exp\left(\frac{-g_0 M_{air} X_3}{R_{gas} T_0}\right)$$
$$P_{atm} = P_0 exp\left(\frac{-g_0 M_{air} X_3}{R_{gas} T_0}\right)$$

Shuttle Orbiter dynamics expressed in terms of states and controls:

$$\dot{X}_1 = -\frac{D}{X_5} - g\sin X_2$$
$$\dot{X}_2 = \frac{L}{X_1 X_5} - \frac{g}{X_1}\cos X_2 + \frac{X_1 \cos X_2}{R_e + X_3}$$
$$\dot{X}_3 = -X_1 \sin X_2$$
$$\dot{X}_4 = \frac{X_1 \cos X_2}{R_e + X_3}$$
$$\dot{X}_5 = \frac{M}{I_{yy}}$$
$$\dot{X}_6 = X_5 + \dot{X}_2 + \dot{X}_4$$

$$D = \tfrac{1}{2}S_{ref}C_D\rho X_1^2$$
$$L = \tfrac{1}{2}S_{ref}C_L\rho X_1^2$$
$$M = \tfrac{1}{2}S_{ref}l_{ref}C_L\rho X_1^2$$

$$C_L = C_{L_0} + C_{L_{\delta_1}} U_1$$
$$C_M = C_{M_0} + C_{M_{\delta_2}} U_2$$

$$g = g_0 \frac{r_E}{(r_E + X_3)^2}$$
$$\rho = \rho_0 exp\left(\frac{-g_0 M_{air} X_3}{R_{gas} T_0}\right)$$

The state to be optimised is the downrange position at the end time, so $J = M = -X_4$ to maximise the downrange distance and $J = M = X_4$ to minimise the downrange distance.

⬛ 7.3.2   Initial guess

For a pseudo-spectral solver, a good initial guess is needed to benefit convergence properties. While this is not as important as with indirect methods, the data being modelled is bumpy with the possibility for many local minima and maxima, at least across the aerodynamic surfaces.

For each state, the initial guess is provided by the solver as calculated as follows.

$$X_{guess} = \frac{X(t_f) - X(t_0)}{t_f - t_0} + X(t_i)$$

⬛ 7.3.3   Bounds

Bounds will be imposed on the control variables and states to limit them to physically reasonable behaviour and to further constrain the system. The velocity is reduced to below $7000 \frac{m}{s}$ to prevent cases where the vehicle would obtain escape velocity and have effectively infinite downrange distance. The velocity is also constrained to being above $1 \frac{m}{s}$ to account for the singularity in the system dynamics when $V = 0$. The flight path angle is between just above 90° and below -90° to constrain the vehicle to forward motion. The altitude is limited to 90 km to prevent skip re-entry which would drastically increase the vehicle range. This is an important consideration but beyond the scope of this investigation. The mass can decrease no further than the value of the structural mass, and the angle of attack is allowed to vary across all angles, as the thrust will be required to be oriented 180° against the direction of motion for a powered descent.

For the states:

$$1 < V < 7000 \frac{m}{s}$$

$$-90.1^o < \gamma < 90.1^o$$
$$-5 < h < 90000m$$
$$-\inf < \theta < \inf$$
$$m_s < m < m_s + m_f$$
$$-\inf < q < \inf$$
$$-180^o < \alpha < 180^o$$

For the controls:

$$-90^o < \delta_1 < 90^o$$
$$-90^o < \delta_2 < 90^o$$
$$-180^o < \alpha < 180^o$$
$$0 < \dot{m}_f < 235\frac{kg}{s}$$

■ 7.3.4 Boundary constraints

The boundary constraints at $t = 0$ define the initial system state and the boundary constraints at $t = t_f$ must define an acceptable landing state. As the two vehicles are designed for different landing conditions, with the LFBB thrusting against its motion to gentle descend on the pad and the Shuttle buffering speed at a high angle of attack and flying along a glide slope to a slow runway approach. This is a time free problem as what matters is whether the vehicle can get to the end location with the appropriate speed, not how long it takes.

The start constraints for each vehicle are therefore

Ariane LFBB	Shuttle Orbiter
$V(0) = V_i$	$V(0) = V_i$
$\gamma(0) = \gamma_i$	$\gamma(0) = \gamma_i$
$h(0) = 80000$	$h(0) = 80000$
$\theta(0) = 0$	$\theta(0) = 0$
$m(0) = m_s + m_f$	$q(0) = 0$
.	$\alpha(0) = 0$

$V(t_f) = 5$	$V(t_f) = 200$
$h(t_f) = 0$	$h(t_f) = 0$
$\gamma(t_f) = 90^o$	

Chapter 8

The flight envelope

8.1 Results

8.1.1 Ariane V LFBB

The optimal control pseudospectral solver was executed with the constraints and Meyer function as elaborated upon in Chapter 7. After a number of iterations, results were obtained for the maximum and minimum possible downrange distance for initial velocities V = [10,100,1000,5000] $\frac{m}{s}$ and initial flight path angles of γ = [0, 30, 60, 90] degrees. The results of those values are tabulated below.

Minimum downrange distance $\theta(t_f)$ (deg)			
	10 $\frac{m}{s}$	100 $\frac{m}{s}$	1000 $\frac{m}{s}$	5000 $\frac{m}{s}$
0°	0.0628	0.0334	0.3612	0.6398
30°	0.0284	0.1163	0.02393	0.2429
60°	0.0299	0.0256	0.1978	0.1669
90°	0.2120	0.1128	0.0502	-*

Table 8.1: Minimum downrange distance $\theta(t_f)$ (deg)

*$5000\frac{m}{s}$ case for 90° did not converge

The general trend of the minimum downrange results is that as the velocity increases, in particular for shallow flight path angles, the minimum possible downrange distance increases. As the vehicle is moving quickly it overshoots landing sites near to its starting point before it reaches the ground, and seems to be unable to be controlled down to those sites. This behaviour is not exhibited in the case of the vehicle entering directed straight down however where the opposite trend is observed. This is likely due to the fact that a vehicle moving very quickly without a shallow flight path angle to experience

more drag experiences the atmosphere essentially as a discontinuity and so the lifting force that would compel it further downrange as it dives is not experienced to the same extent.

The final velocity for each sample case is the prescribed $5\frac{m}{s}$, the final altitude is the prescribed 0m, and the flight path angle is 90°, indicating that the solver has obeyed the constraints for each test. The final time of flight and number of solutions before solver convergence are also provided.

Minimum downrange time of flight t(s)				
	$10\ \frac{m}{s}$	$100\ \frac{m}{s}$	$1000\ \frac{m}{s}$	$5000\ \frac{m}{s}$
0°	251	167	255	265
30°	193	334	217	150
60°	180	171	244	149
90°	327	220	182	-

Table 8.2: Minimum downrange time of flight t(s)

Minimum downrange solver iterations				
	$10\ \frac{m}{s}$	$100\ \frac{m}{s}$	$1000\ \frac{m}{s}$	$5000\ \frac{m}{s}$
0°	494	376	131	225
30°	427	336	268	440
60°	312	480	162	152
90°	280	127	187	-

Table 8.3: Minimum downrange solver iterations

An example of the control surface deflections and state output for the solver is provided for the test case of $V_0 = 100\frac{m}{s}$, $\gamma_o = 30^o$

The results for the maximum downrange distance are now provided. As expected, the maximum downrange distance is greater than the minimum for each test case. As can be seen there is a general trend where increasing the starting velocity increases the final downrange distance and increasing the flight path angle decreases it, which is intuitive. The results are less compliant to this trend in this case, particularly noticeable for the $100\frac{m}{s}$ tests. ,

As can be seen from the results, while some general trends are present, there is a lot of variation from test to test. Because a limited number of nodes was used in this solver to drastically reduce the computation time it is suggested that the accuracy and optimality of the results is lower than ideal. For comparison, the number of nodes used in a similar study of optimal re-entry trajectories was 20 for a low fidelity solution and 80 for a high fidelity solution.[5] The number of nodes in this test should be increased to 20 and then compared to the present results to note any discrepancies. The control signal and state evolution for the same case as the minimum downrange distance is provided again.

Control signal for min downrange case: $V_0 = 100\frac{m}{s}$, $\gamma_0 = 30^o$			
t (s)	$\dot{m}\frac{m}{s}$	α (rad)	δ (rad)
0	62.452	3.142	-1.000
11	8.473	-2.058	-0.165
42	53.970	-1.571	0.097
83	176.498	-2.842	-0.165
125	18.090	2.729	0.292
156	35.815	-2.981	-0.053
167	235.000	-0.185	0.190
167	235.000	3.142	0.243
178	194.572	0.228	-0.088
208	235.000	-0.293	0.255
250	220.541	2.901	0.225
293	35.760	-0.097	0.308
323	0.000	-3.022	1.000
334	53.706	0.888	-1.000

Table 8.4: Control signal for min downrange case: $V_0 = 100\frac{m}{s}$, $\gamma_0 = 30^o$

State evolution for min downrange case: $V_0 = 100\frac{m}{s}$, $\gamma_0 = 30^o$					
t (s)	V $\frac{m}{s}$	γ (rad)	h (m)	θ (rad)	m (kg)
0	100.0	0.52	80000.0	1.20E-16	237700
11	159.5	0.91	78999.3	1.67E-04	237195
42	335.8	1.49	72117.0	4.85E-04	237621
83	639.8	1.59	51207.5	4.65E-04	236524
125	513.7	1.54	24958.9	4.89E-04	232023
156	182.8	1.59	14491.2	5.22E-04	224123
167	150.3	1.59	12728.6	5.14E-04	222536
167	150.3	1.59	12728.6	5.14E-04	222536
178	175.6	0.64	11339.4	6.67E-04	220616
208	113.1	1.59	8243.9	1.11E-03	214831
250	114.5	1.44	3096.4	8.61E-04	212669
293	161.3	0.15	139.3	1.63E-03	211847
323	3.6	-1.43	-1.0	2.05E-03	211910
334	5.0	1.57	0.0	2.03E-03	211619

Table 8.5: State evolution for min downrange case: $V_0 = 100\frac{m}{s}$, $\gamma_0 = 30^o$

8.1.2 Shuttle Orbiter

The results for the Shuttle Orbiter had difficultly converging and so have not been able to be provided in time.

It is suggested that scaling the state variables to between 0 and 1 will likely significantly improve convergence properties, especially for a re-entry scenario like the Shuttle Orbiter with fast moving rotational modes from

Maximum downrange distance $\theta(t_f)$ (deg)			
	$10\ \frac{m}{s}$	$100\ \frac{m}{s}$	$1000\ \frac{m}{s}$	$5000\ \frac{m}{s}$
0°	0.362	0.186	1.402	1.004
30°	0.333	0.225	0.643	0.559
60°	0.181	0.591	0.260	0.305
90°	-*	0.262	0.275	-*

Table 8.6: Maximum downrange distance $\theta(t_f)$ (deg)

Maximum downrange iteration count			
	$10\ \frac{m}{s}$	$100\ \frac{m}{s}$	$1000\ \frac{m}{s}$	$5000\ \frac{m}{s}$
0°	195	228	383	487
30°	186	91	428	371
60°	66	499	195	235
90°	-*	157	181	-*

Table 8.7: Maximum downrange solver iterations

Control signal for max downrange case: $V_0 = 100\frac{m}{s}$, $\gamma_0 = 30^o$			
t (s)	$\dot{m}\frac{m}{s}$	α (rad)	δ (rad)
0	85	0.06	0.97
11	31	-2.32	1.00
40	190	-3.14	1.00
80	233	-3.13	1.00
121	107	-2.68	0.42
150	192	-1.57	0.29
161	233	1.24	-0.40
161	2	2.54	0.85
172	221	-3.14	0.17
201	0	-2.87	-0.16
241	14	-3.14	0.07
282	233	0.02	0.09
311	13	-1.47	0.99
322	26	0.20	-1.00

Table 8.8: Control signal for max downrange case: $V_0 = 100\frac{m}{s}$, $\gamma_0 = 30^o$

the flap induced moment and much slower dynamical modes from the kinematics and change of altitude.[5] For re-entry problems, it is common to non-dimensionalise the problem using the modified Chapman equations.[37] Alternatively, scale factors for mass, time, length can be introduced and used to non-dimensionalise the problem. This scaling should in future be introduced into the equations of motion.

State evolution for max downrange case: $V_0 = 100\frac{m}{s}$, $\gamma_0 = 30^o$					
t (s)	V $\frac{m}{s}$	γ (deg)	h (m)	θ (deg)	m (kg)
0	100	0.524	80000	1.51E-20	237700
11	181	1.129	78796	1.39E-04	237184
40	313	1.494	71450	3.78E-04	234314
80	436	1.542	56265	4.17E-04	224430
121	450	1.253	38120	8.56E-04	218044
150	326	1.063	27489	1.63E-03	214017
161	253	1.243	24684	1.84E-03	211707
161	253	1.243	24684	1.84E-03	211707
172	232	0.795	22593	2.07E-03	210207
201	241	1.555	17035	2.51E-03	205857
241	253	1.341	6122	2.45E-03	208363
282	194	0.234	247	3.43E-03	201631
311	14	-0.325	-1	3.93E-03	197767
322	5	1.571	0	3.93E-03	197700

Table 8.9: State evolution for max downrange case: $V_0 = 100\frac{m}{s}$, $\gamma_0 = 30^o$
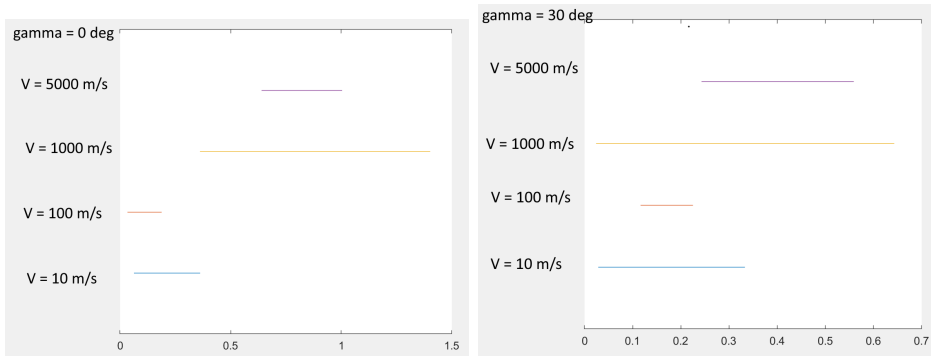
Figure 8.1: Flight envelopes for $\gamma_0 = 0^o, 30^o$
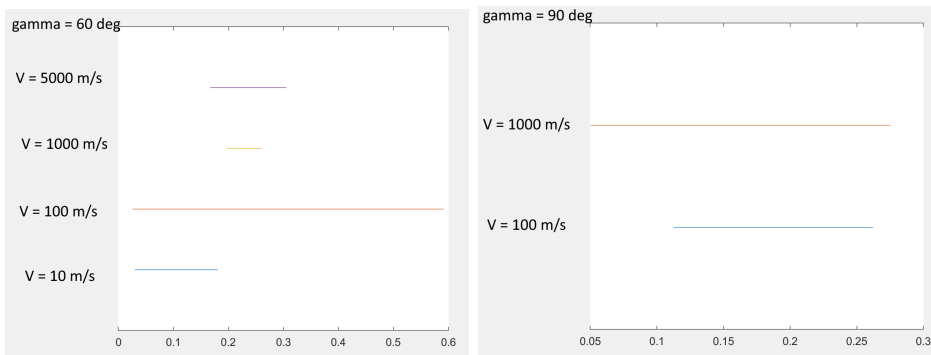
Figure 8.2: Flight envelopes for $\gamma_0 = 60^o, 90^o$

Chapter 9

Validation of results

To validate the results a feasibility analysis will be conducted to ensure that the dynamics can actually reach the states suggested by the optimal solution path, and an optimality test will be conducted to check if the suggested optimum path is actually optimum.

To test the feasibility the control signal can be fed into the ODE45 state propagator for the model to be tested with the same start conditions. If the trajectories are approximately the same, then the result is feasible.[5]

For the optimality, Bellman's Principle of Optimality will be employed. The suggestion of this principle is that if one point on the optimum trajectory is selected as the new initial condition, the the resulting trajectory to the final boundary should be the same as with the earlier initial condition.[5]

The trajectory to be tested will be the control inputs from the optimal trajectory for the maximum downrange case, for $V = 100\frac{m}{s}$, $\gamma = 30^o$.

9.1   Feasibility analysis

The optimal and actual propagated trajectories are plotted below for a number of important states.

As can be seen, while the general form of the trajectory is followed there is quite a bit of error between the optimal and actual trajectories. The low node code used in generating the optimal trajectory may contribute to the very approximate nature of the optimal trajectory. This feasibility test should be repeated for an optimal trajectory generated with a higher resolution.
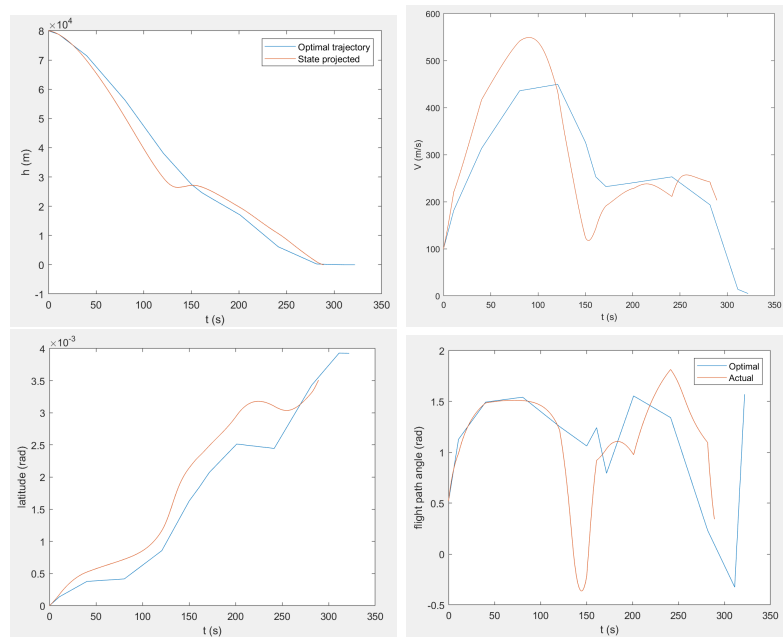
Figure 9.1: Feasible vs optimal trajectory for altitude, velocity, latitude, flight path angle.

■ 9.2   Bellman test of optimality

The initial conditions for the test case are:

$[V, \gamma, h, \theta, m] = [100, 0.524, 80000, 0, 237700]$

This generates a point in the trajectory at t = 80.5 with the states:

$[V, \gamma, h, \theta, m] = [436, 1.542, 56265, 4.16e - 04, 224430]$

that will be used as the new initial condition.

As for the previous test, the general trends are followed however there is quite a bit of variability. In particular, the final calculated downrange distance varies notably. This suggests that the optimality of the trajectories generated in this report may not be high. Again, a higher node experiment is recommended.
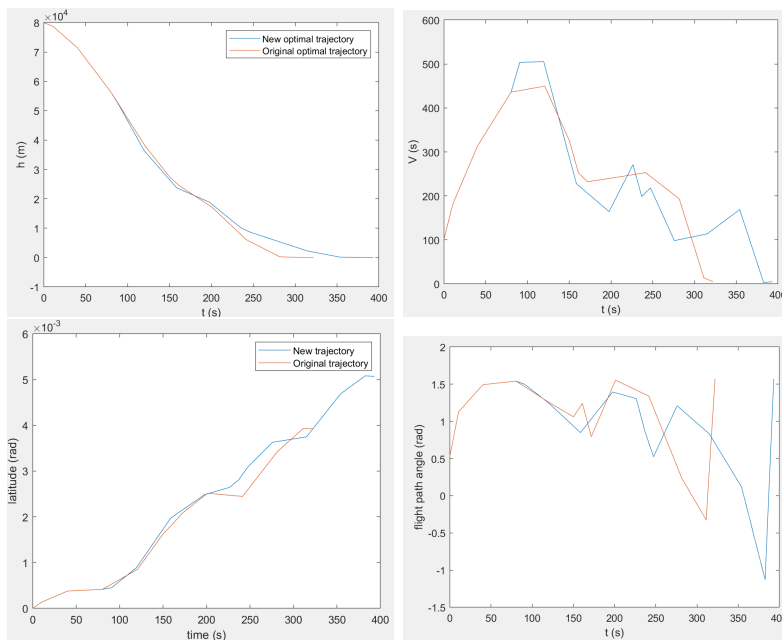
Figure 9.2: Both the original and new optimal trajectory for altitude, velocity, latitude, flight path angle.

Chapter 10

Conclusion

A set of landable states has been generated for the Ariane V LFFB concept using Daniel Herber's pseudo-spectral optimization routine. The Shuttle Orbiter was found to have poor convergence properties and so cannot be included in this report. Models were established of the atmosphere, vehicle properties, Earth, and the aerodynamics which were investigated in detail. The aerodynamic model was fitted to curves using TableCurve3D to avoid discontinuities in the data and so that it could be used in the state propagator ODE45 and the optimization routine. The aerodynamic model was validated against the re-entry trajectory software HyperSMS and conformed well to the expected behaviour.

There is a general trend that increasing the re-entry velocity and making the flight path more shallow should increase the maximum possible downrange distance and decrease the minimum possible distance, which is an intuitive result. There seems to be a high degree of variability over this trend however, calling into question the validity of the results. Indeed due to poor similarity of the trajectories when using the feasibility and optimality test this assumption seems to be founded. It is suggested that the number of nodes used in executing the optimization problem should be increased, although this will greatly increase the computational resources required. Scaling of the problem should improve the convergence properties, and so this should be included in future work.

Bibliography

[1] Tablecurve 3d automated surface fitting software. *Jandel Scientific*, 1993.

[2] H Julian Allen and Edward W Perkins. *Characteristics of flow over inclined bodies of revolution*. National Advisory Committee for Aeronautics, 1951.

[3] US Standard Atmosphere. *US standard atmosphere*. National Oceanic and Atmospheric Administration, 1976.

[4] John T Betts and William P Huffman. Path-constrained trajectory optimization using sparse sequential quadratic programming. *Journal of Guidance, Control, and Dynamics*, 16(1):59–68, 1993.

[5] Kevin P Bollino. High-fidelity real-time trajectory optimization for reusable launch vehicles. Technical report, NAVAL POSTGRADUATE SCHOOL MONTEREY CA DEPT OF MECHANICAL AND ASTRONAUTICAL . . . , 2006.

[6] John V Breakwell, Jason L Speyer, and Arthur E Bryson. Optimization and control of nonlinear systems using the second variation. *Journal of the Society for Industrial and Applied Mathematics, Series A: Control*, 1(2):193–223, 1963.

[7] Sheung Sher Chin. Missile configuration design. 1961.

[8] RF Clippinger, JH Giese, and WC Carter. Tables of supersonic flows about cone cylinders. part 1. surface data. Technical report, Army Ballistic Research Lab Aberdeen Proving Ground MD, 1950.

[9] B LOUIS Decker. World geodetic system 1984. Technical report, Defense Mapping Agency Aerospace Center St Louis Afs Mo, 1986.

[10] Walter F Denham and Arthur E Bryson Jr. Optimal programming problems with inequality constraints. ii-solution by steepest-ascent. *AIAA Journal*, 2(1):25–34, 1964.

[11] James Diebel. Representing attitude: Euler angles, unit quaternions, and rotation vectors. *Matrix*, 58(15-16):1–35, 2006.

[12] Th. Eggers and Ognjan Bozic. Aerodynamic design and analysis of an ariane 5 liquid flyback booster. 1999.

[13] Dorris M Ehret, Vernon J Rossow, and Victor I Stevens. An analysis of the applicability of the hypersonic similarity law to the study of flow about bodies of revolution at zero angle of attack. 1950.

[14] Paolo Francesco Scaramuzzino et al. Hypersms aerothermodynamic tool user's guide, 2015.

[15] John C Evvard. Distribution of wave drag and lift in the vicinity of wing tips at supersonic speeds. Technical report, Flight Propulsion Research Lab Cleveland OH, 1947.

[16] F Frankl and V Voishel. Turbulent friction in the boundary layer of a flat plate in a two-dimensional compressible flow at high speeds. 1943.

[17] Charles R Hargraves and Stephen W Paris. Direct trajectory optimization using nonlinear programming and collocation. *Journal of guidance, control, and dynamics*, 10(4):338–342, 1987.

[18] Martin Hepperle. Javafoil. *Retrieved from Aerodynamics of Model Aircraft: http://www.mh-aerotools.de/airfoils/javafoil.htm*, 2007.

[19] Daniel Ronald Herber. Basic implementation of multiple-interval pseudospectral methods to solve optimal control problems. Technical report, 2015.

[20] Finck RD et al. Hoak, DE. Control datcom. *Air Force Flight Dynamics Laboratory, Wright-Patterson Air Force Base, Ohio*, 1978.

[21] Yoshiyuki Ishijima, Shuichi Matsumoto, and Kentaro Hayashi. Re-entry and terminal guidance for vertical-landing tsto (two-stage to orbit). In *Guidance, Navigation, and Control Conference and Exhibit*, page 4120, 1998.

[22] Leland H Jorgensen. *Inclined bodies of various cross sections at supersonic speeds*, volume 10. NASA, 1958.

[23] Nikolaǐ Krasnov. *Rocket aerodynamics*.

[24] FG Lemoine, SC Kenyon, JK Factor, RG Trimmer, NK Pavlis, DS Chinn, CM Cox, SM Klosko, SB Luthcke, MH Torrence, et al. The development of the joint nasa gsfc and the national imagery and mapping agency (nima) geopotential model egm96. 1998.

[25] Brent Lewis. Us standard atmosphere. 2020.

[26] Angelo Miele and Carlos R Cavoti. Variational approach to the re-entry of a ballistic missile. part i. Technical report, Purdue University LaFayette in School of Aeronautics and Astronautics, 1959.

[27] Edward Roy Cecil Miles. *Semi-empirical Formulas for Ogives.* Johns Hopkins University, 1948.

[28] Michael Mistry. Robot learning and sensorimotor control, 2018.

[29] Max M Munk. The aerodynamic forces on airship hulls. 1924.

[30] PRESIDENTIAL COMMISSION on the Space Shuttle Challenger Accident. Volume 2: Enclosure 8: Space transportation system, mission 51-l structural reconstruction and evaluation report, 1986.

[31] Hans Josef Pesch. Neighboring optimum guidance of a space-shuttle-orbiter-type vehicle. *Journal of Guidance and Control*, 3(5):386–391, 1980.

[32] Michael J Policelli. Vertical takeoff vertical landing spacecraft trajectory optimization via direct collocation and nonlinear programming, 2014.

[33] Frank J Regan and Satya M Anandakrishnan. *Dynamics of atmospheric re-entry.* American Institute of Aeronautics and Astronautics, 1993.

[34] Bernard F Saffell Jr, Millard L Howard, and Eugene N Brooks Jr. Method for predicting the static aerodynamic characteristics of typical missile configurations for angles of attack to 180 degrees. Technical report, DAVID W TAYLOR NAVAL SHIP RESEARCH AND DEVELOPMENT CENTER BETHESDA MD, 1971.

[35] Martin Sippel and Josef Klevanski. Preliminary definition of an aerodynamic configuration for a reusable booster stage within tight geometric constraints. 8(11), 2004.

[36] Milton D Van Dyke. A study of second-order supersonic flow theory. 1952.

[37] Nguyen X Vinh. Optimal trajectories in atmospheric flight. Elsevier, 1981.

[38] Henryk Kazimierz Zienkiewicz. *A Method for Calculating Pressure Distributions on Circular Arc Ogives at Zero Incidence at Supersonic Speeds, Using the Prandtl-Meyer Flow Relations.* HM Stationery Office, 1953.

Chapter 11

Appendix – Curve fits

Rank 2 Eqn 1408 Chebyshev X,Y Rational Order 8/9

r² Coef Det	DF Adj r²	Fit Std Err	F-value
0.9610067246	0.9604913301	0.0802729501	1920.170315

Parm	Value	Std Error	t-value	95.00% Confidence Limits		P>|t|
a	-0.23904036	0.0038079	-62.7748542	-0.24650712	-0.2315736	0.00000
b	0.374114442	0.018459295	20.26699517	0.33791835	0.410310533	0.00000
c	1.48757e-19	0.015119593	9.8387e-18	-0.0296474	0.029647405	1.00000
d	-0.12580021	0.006748266	-18.6418559	-0.13903261	-0.1125678	0.00000
e	-1.4252e-20	0.003500056	-4.0719e-18	-0.00686312	0.006863119	1.00000
f	0.040854248	0.019164387	2.131779543	0.00327557	0.078432925	0.03312
g	0.207318199	0.015968167	12.98321835	0.176006861	0.238629538	0.00000
h	-0.03533506	0.006634744	-5.32576155	-0.04834487	-0.02232526	0.00000
i	0.124140439	0.005933657	20.92140355	0.112505368	0.13577551	0.00000
j	0.141364612	0.01593388	8.87195178	0.110120506	0.172608718	0.00000
k	1.36402e-19	0.013554489	1.00632e-17	-0.02657845	0.026578453	1.00000
l	0.014406527	0.006024669	2.391256278	0.002592995	0.026220058	0.01686
m	-3.0077e-20	0.003401595	-8.8419e-18	-0.00667005	0.006670051	1.00000
n	0.109893431	0.013286402	8.271120602	0.083840659	0.135946204	0.00000
o	0.121903951	0.013856059	8.797880758	0.094734161	0.149073741	0.00000
p	-0.10257872	0.005162273	-19.8708436	-0.11270122	-0.09245623	0.00000
q	-0.18644407	0.005007381	-37.2338474	-0.19626284	-0.17662529	0.00000
r	-0.17354721	0.012624401	-13.7469663	-0.19830189	-0.14879253	0.00000
s	5.78781e-20	0.01034259	5.59609e-18	-0.02028037	0.02028037	1.00000
t	0.091552371	0.005054358	18.11355173	0.081641484	0.101463259	0.00000
u	-1.4701e-20	0.003114787	-4.7196e-18	-0.00610766	0.006107661	1.00000
v	-0.01499011	0.015156118	-0.98904685	-0.04470914	0.014728914	0.32273
aa	0.038519663	0.009344925	4.121987209	0.020195573	0.056843753	0.00004
ab	0.011355967	0.005684868	1.997578069	0.000208738	0.022503197	0.04586
ac	0.001001146	0.004117541	0.243141837	-0.00707277	0.009075067	0.80791
ad	-0.1726987	0.017381046	-9.93603635	-0.2067805	-0.13861691	0.00000
ae	4.49135e-20	0.009006179	4.98697e-18	-0.01765986	0.017659855	1.00000
af	0.026855049	0.006331587	4.241440446	0.014439694	0.039270404	0.00002
ag	-2.8592e-20	0.003087717	-9.26e-18	-0.00605458	0.006054581	1.00000
ah	-0.23393592	0.016069752	-14.5575314	-0.26544646	-0.20242539	0.00000
ai	0.007705698	0.007094689	1.086121918	-0.00620599	0.02161739	0.27752
aj	0.09545944	0.005046045	18.9176761	0.085564853	0.105354027	0.00000
ak	-0.02289071	0.003542749	-6.46128651	-0.02983755	-0.01594388	0.00000
al	-0.03423153	0.009814395	-3.4878901	-0.05347618	-0.01498688	0.00049
am	1.90015e-21	0.006470739	2.93652e-19	-0.01268821	0.012688212	1.00000

Figure 11.1: Ariane drag coefficients for Eqn1408 Chebyshev fit.

Rank 2 Eqn 1408 Chebyshev X,Y Rational Order 8/9

	r² Coef Det	DF Adj r²	Fit Std Err	F-value		
	0.9966876934	0.9966439129	0.0318882009	23443.994248		

Parm	Value	Std Error	t-value	95.00% Confidence Limits		P>|t|
a	-0.05508136	0.0023124	-23.8199934	-0.05961565	-0.05054706	0.00000
b	0.598786981	0.01372823	43.61720247	0.571867845	0.625706117	0.00000
c	0.048713521	0.041004508	1.188004038	-0.03169058	0.129117616	0.23494
d	-0.05916188	0.002610267	-22.6650668	-0.06428024	-0.05404351	0.00000
e	0.156842173	0.004691522	33.43098189	0.147642756	0.166041589	0.00000
f	-0.06473138	0.013492521	-4.79757518	-0.09118833	-0.03827444	0.00000
g	0.150719974	0.02411025	6.251282117	0.103443151	0.197996797	0.00000
h	0.006925127	0.001783094	3.883769805	0.003428729	0.010421525	0.00011
i	-0.03709317	0.003323259	-11.161685	-0.04360962	-0.03057673	0.00000
j	-0.04619282	0.011104446	-4.15984889	-0.06796708	-0.02441855	0.00003
k	-0.11916067	0.027822725	-4.28285389	-0.17371713	-0.0646042	0.00002
l	0.002692529	0.001623098	1.65888258	-0.00049014	0.005875197	0.09726
m	-0.1509388	0.00570049	-26.4782136	-0.16211667	-0.13976094	0.00000
n	0.061291411	0.00864704	7.088137954	0.044335777	0.078247045	0.00000
o	0.079302304	0.018800356	4.218127819	0.04243744	0.116167168	0.00003
p	-0.01107764	0.001389726	-7.97109873	-0.0138027	-0.00835258	0.00000
q	-0.07828682	0.002705319	-28.9381155	-0.08359157	-0.07298207	0.00000
r	-0.04573438	0.008438711	-5.41959371	-0.06228151	-0.02918725	0.00000
s	-0.06626214	0.019476943	-3.402081	-0.1044537	-0.02807058	0.00068
t	0.008355606	0.001414424	5.907427631	0.005582119	0.011129093	0.00000
u	0.013381364	0.003278168	4.081963548	0.006953335	0.019809394	0.00005
v	0.004432392	0.01037313	0.427295493	-0.01590786	0.024772647	0.66920
aa	0.036333875	0.009592036	3.787921054	0.017525236	0.055142514	0.00016
ab	-0.00110031	0.001547151	-0.71118707	-0.00413406	0.001933433	0.47703
ac	0.01440614	0.002478287	5.81294321	0.009546567	0.019265713	0.00000
ad	-0.01041563	0.012980208	-0.80242367	-0.035868	0.015036744	0.42238
ae	-0.02497775	0.008735887	-2.85921144	-0.0421076	-0.0078479	0.00428
al	0.003957609	0.001738864	2.275974066	0.000547941	0.007367278	0.02293
ag	0.006432527	0.002467078	2.607347007	0.001594934	0.011270121	0.00918
ah	-0.03005306	0.011986858	-2.50716751	-0.05355761	-0.00654851	0.01223
ai	0.016401215	0.004748969	3.453636824	0.007089152	0.025713279	0.00056
aj	0.00936001	0.001447041	6.468379234	0.006522565	0.012197454	0.00000
ak	0.000275004	0.00232163	0.118452835	-0.00427739	0.004827394	0.90572
al	0.029512237	0.006570282	4.491776253	0.016628834	0.042395639	0.00001
am	-0.0115452	0.004431997	-2.60496659	-0.02023573	-0.00285468	0.00924

Figure 11.2: Ariane lift coefficients for Eqn1408 Chebyshev fit.

Parm	Value	Std Error	t-value	95.00% Confidence Limits		P>|t|
a	0.346462412	0.017732213	19.53858808	0.311691905	0.381232919	0.00000
b	0.729795048	0.179959917	4.055319978	0.376917632	1.082672465	0.00005
c	-0.55115008	0.195153206	-2.82419178	-0.93381951	-0.16848065	0.00478
d	0.085848163	0.058440728	1.468978325	-0.02874632	0.200442644	0.14196
e	-0.00547213	0.203060409	-0.02694827	-0.40364653	0.392702276	0.97850
f	0.104837714	0.06608789	1.586337745	-0.02475183	0.234427259	0.11278
g	-0.65480616	0.074301118	-8.81287089	-0.80050075	-0.50911157	0.00000
h	-0.56278749	0.099337717	-5.66539589	-0.75757552	-0.36799947	0.00000
i	0.058020695	0.185738813	0.312377872	-0.30618836	0.422229755	0.75478
j	-0.20695257	0.071652226	-2.8882922	-0.34745303	-0.0664521	0.00391
k	0.574656062	0.109169757	5.263876008	0.360588718	0.788723407	0.00000
l	0.509554821	0.121285431	4.201286301	0.271730253	0.74737939	0.00003
m	0.082622457	0.108605259	0.760759271	-0.13033798	0.295582897	0.44687
n	-0.31810917	0.202422084	-1.57151416	-0.7150319	0.078813561	0.11618
o	0.100128689	0.083487702	1.199322617	-0.06357957	0.263836948	0.23051
p	-0.64191172	0.111984892	-5.73212788	-0.86149917	-0.42232427	0.00000
q	0.40169632	0.143350733	2.802192293	0.120604635	0.682788004	0.00511
r	0.091494104	0.204442291	0.447530221	-0.30938999	0.492378192	0.65453
s	-0.55314455	0.157241071	-3.51781217	-0.86147334	-0.24481577	0.00044
t	0.447130508	0.16966244	2.635412451	0.114445071	0.779815945	0.00845
u	0.038108765	0.076625064	0.497340724	-0.11214277	0.188360304	0.61899
v	0.351998859	0.099331907	3.543663569	0.157222227	0.54677549	0.00040
aa	-0.64560847	0.127599027	-5.05966607	-0.89581316	-0.39540378	0.00000
ab	-0.41255338	0.262871992	-1.5694079	-0.92801033	0.102903564	0.11667
ac	1.076234699	0.283830324	3.791824222	0.519681256	1.632788141	0.00015
ad	0.567481261	0.1533347	3.700931762	0.266812348	0.868150174	0.00022
ae	-0.36240467	0.131798771	-2.74968173	-0.6208445	-0.10396485	0.00601
af	0.203144327	0.067118664	3.026644387	0.071533572	0.334755082	0.00250
ag	-0.35448623	0.081629915	-4.34260194	-0.51455161	-0.19442084	0.00001
ah	0.431823548	0.118420294	3.646533323	0.199617132	0.664029963	0.00027
ai	0.452098655	0.225332586	2.006361632	0.010251481	0.893945828	0.04492
aj	-0.58770756	0.318380365	-1.84592903	-1.21200903	0.03659391	0.06501
ak	-0.91468647	0.238870434	-3.82921595	-1.38307956	-0.44629339	0.00013
al	-0.04914921	0.121936705	-0.40307151	-0.28825084	0.189952418	0.68693
am	0.464562965	0.100567369	4.619420507	0.267363756	0.661762173	0.00000
an	0.339802335	0.057689499	5.890193862	0.226680914	0.452923755	0.00000
ao	0.038636621	0.042981401	0.898914875	-0.04564418	0.12291742	0.36878
ap	-0.25123944	0.084381842	-2.97741119	-0.41670099	-0.08577789	0.00293
aq	-0.44702177	0.152458398	-2.93209015	-0.74597237	-0.14807116	0.00340
ar	0.443284011	0.22086292	2.007054926	0.010201258	0.876366764	0.04485
as	0.285230207	0.21529909	1.324890163	-0.13694262	0.707403032	0.18535
at	-0.16190202	0.144370366	-1.12143527	-0.44499307	0.121189028	0.26221
au	0.493337547	0.077013563	6.405852775	0.342324213	0.644350882	0.00000
av	-0.36411861	0.065476698	-5.56104109	-0.49250969	-0.23572753	0.00000
ba	-0.11637405	0.036202608	-3.21452108	-0.18736254	-0.04538556	0.00132
bb	-0.18303093	0.049293823	-3.71306018	-0.27968955	-0.08637231	0.00021
bc	-0.0701726	0.065859456	-1.06549006	-0.19931421	0.058969021	0.28675
bd	0.248571838	0.079258142	3.136230956	0.093157184	0.403986493	0.00173
be	0.032258345	0.107443385	0.300235746	-0.17842382	0.242940505	0.76402
bf	-0.39274082	0.108430337	-3.62205657	-0.60535826	-0.18012337	0.00030
bg	0.444581081	0.095631271	4.648909061	0.257060903	0.632101259	0.00000
bh	-0.73929709	0.061731087	-11.9760906	-0.86034352	-0.61825065	0.00000
bi	0.037771194	0.046045622	0.820299368	-0.05251813	0.128060522	0.41212
bj	0.296764809	0.047101932	6.300480594	0.204404197	0.389125421	0.00000
bk	0.105489365	0.046422033	2.272398633	0.014461944	0.196516787	0.02314

Figure 11.3: Ariane moment coefficients for Eqn608 Sigmoid fit.

79

Rank 1 Eqn 524 Fourier Series Bivariate Order 2x5

r^2 Coef Det	DF Adj r^2	Fit Std Err	F-value
0.8507420075	0.8472695676	0.2342063604	249.17663801

Parm	Value	Std Error	t-value	95.00% Confidence Limits		P>|t|
a	157.2356816	10.56829139	14.87806078	136.5126487	177.9587145	0.00000
b	3.171584829	2.322308484	1.365703502	-1.38215744	7.725327094	0.17215
c	1.8109e-12	1.807441959	1.00191e-12	-3.54415655	3.544156554	1.00000
d	-266.404173	16.59487263	-16.0534027	-298.944541	-233.863805	0.00000
e	12.98328418	10.53019602	1.232957502	-7.66504872	33.63161708	0.21770
f	-184.090155	10.98861877	-16.752802	-205.637395	-162.542915	0.00000
g	-12.3067652	6.512511243	-1.88971117	-25.0769454	0.463414913	0.05891
h	-4.50650485	2.045590142	-2.20303411	-8.51763875	-0.49537095	0.02768
i	-8.2967e-13	1.109764304	-7.476e-13	-2.17610221	2.176102206	1.00000
j	-3.02943325	1.555396675	-1.94769174	-6.07936207	0.020495568	0.05156
k	-4.4661e-13	0.734044532	-6.0842e-13	-1.43936503	1.439365026	1.00000
l	94.71200017	5.526679799	17.13723313	83.87490615	105.5490942	0.00000
m	4.821002596	3.183512789	1.514365707	-1.42144833	11.06345352	0.13005
n	33.91761325	1.905001076	17.80451133	30.18215606	37.65307043	0.00000
o	1.792620235	1.090623233	1.643665916	-0.34594884	3.931189312	0.10037
p	1.096277138	0.773435141	1.417413148	-0.4203277	2.612881975	0.15648
q	1.82371e-13	0.339841842	5.36636e-13	-0.66638527	0.666385267	1.00000
r	0.434152332	0.201502694	2.154573342	0.039031986	0.829272678	0.03129
s	3.91522e-14	0.086230128	4.54043e-13	-0.16908597	0.169085969	1.00000
t	-6.64193086	0.351813565	-18.879121	-7.3317911	-5.95207061	0.00000
u	-0.420697	0.206443897	-2.03782726	-0.8255064	-0.0158876	0.04167
v	-1.9312e-13	0.38266368	-5.0466e-13	-0.75035327	0.750353273	1.00000
aa	-2.39961366	3.310368267	-0.72487816	-8.89081154	4.091584209	0.46859
ab	-2.6206e-12	2.954767074	-8.8692e-13	-5.79391059	5.793910586	1.00000
ac	-1.52594743	2.050812772	-0.74406959	-5.54732222	2.495427366	0.45690
ad	-1.5459e-12	1.842691959	-8.3893e-13	-3.61327718	3.613277181	1.00000
ae	1.22497e-13	0.378750693	3.23425e-13	-0.74268042	0.74268042	1.00000
af	1.72053e-13	0.364879363	4.71533e-13	-0.71548056	0.715480562	1.00000
ag	7.07159e-14	0.249576896	2.83343e-13	-0.48938755	0.48938755	1.00000
ah	1.13984e-13	0.247075554	4.61333e-13	-0.48448275	0.484482747	1.00000
ai	0.012970577	0.878260543	0.014768484	-1.70918313	1.735124281	0.98822
aj	6.32712e-13	0.79703333	7.93834e-13	-1.5628778	1.562877795	1.00000
ak	0.00461791	0.208697838	0.022127255	-0.40461117	0.413846991	0.98235
al	1.38314e-13	0.192213403	7.19584e-13	-0.37690527	0.376905266	1.00000
am	-2.2882e-14	0.087638211	-2.6109e-13	-0.17184703	0.171847034	1.00000
an	-4.0431e-14	0.092707801	-4.3612e-13	-0.18178784	0.181787835	1.00000
ao	-41.9304269	10.6673358	-3.93073094	-62.8476729	-21.0131809	0.00009
ap	6.829109449	4.937561599	1.383093519	-2.85280107	16.51101997	0.16675
aq	-27.9771475	5.214056717	-5.36571598	-38.2012286	-17.7530663	0.00000
ar	7.13977e-13	1.25083029	5.70803e-13	-2.4527141	2.452714097	1.00000
as	3.311128212	1.453075937	2.278702804	0.461836934	6.16041949	0.02276
at	2.13385e-13	0.560064259	3.81002e-13	-1.09821254	1.098212536	1.00000
au	1.188076159	0.66513364	1.786221725	-0.11616365	2.492315966	0.07418
av	0.167738203	1.810971984	0.092623301	-3.38334027	3.718816676	0.92621
ba	14.69748712	1.976894865	7.434632659	10.82105565	18.5739186	0.00000
bb	0.1156182	0.396144037	0.291858993	-0.66116828	0.892404684	0.77042
bc	3.929544147	0.433578048	9.06306066	3.079354478	4.779733816	0.00000
bd	-4.4526e-14	0.166352249	-2.6766e-13	-0.32619494	0.326194936	1.00000
be	0.567392111	0.209122084	2.713209916	0.15733114	0.977453081	0.00671
bf	4.258760237	1.654177853	2.574547973	1.015134485	7.502385988	0.01009
bg	2.87646e-13	0.580065363	4.95885e-13	-1.13743208	1.137432077	1.00000
bh	2.218647476	0.669765746	3.312572327	0.905324717	3.531970234	0.00094
bi	4.0588e-14	0.151052048	2.68702e-13	-0.29619325	0.296193248	1.00000
bj	1.165412893	0.177330571	6.571979576	0.817690907	1.513134879	0.00000
bk	-0.12986675	0.357696271	-0.36306432	-0.83126221	0.571528708	0.71659
bl	-0.84453719	0.401554198	-2.10317112	-1.63193229	-0.05714209	0.03555
bm	-4.6407e-14	0.188440051	-2.4627e-13	-0.36950622	0.369506219	1.00000
bn	-1.2171e-14	0.080810192	-1.5061e-13	-0.15845818	0.158458184	1.00000
bo	-1.6737e-14	0.075590711	-2.2142e-13	-0.14822347	0.148223467	1.00000
bp	-0.06294882	0.191361221	-0.32895286	-0.43818307	0.312285427	0.74222
bq	-6.9953e-14	0.171170527	-4.0867e-13	-0.33564295	0.335642946	1.00000

Figure 11.4: Shuttle drag coefficients for Eqn524 Fourier fit.

Eqn 1408 Chebyshev X,Y Rational Order 8/9

r² Coef Det	DF Adj r²	Fit Std Err	F-value	
0.9965471773	0.9965015395	0.0381982188	22486.746468	

Parm	Value	Std Error	t-value	95.00% Confidence Limit	
a	-0.05309279	0.002754727	-19.2733431	-0.05849442	-0.04769116
b	0.614436096	0.016581004	37.05662852	0.58192307	0.646949122
c	0.076511937	0.048442222	1.579447314	-0.01847647	0.171500348
d	-0.06180211	0.003138484	-19.6917064	-0.06795624	-0.05564799
e	0.149281291	0.005630964	26.51078984	0.138239761	0.160322822
f	-0.0521019	0.016325639	-3.19141597	-0.08411419	-0.02008961
g	0.151367784	0.028699698	5.274194375	0.095091697	0.20764387
h	0.006467319	0.00212721	3.040281767	0.002296157	0.010638481
i	-0.03877016	0.003988034	-9.72162236	-0.04659014	-0.03095018
j	-0.05351191	0.013551495	-3.94878278	-0.08008449	-0.02693933
k	-0.11119824	0.032902045	-3.3796755	-0.17571454	-0.04668193
l	0.003620217	0.001946734	1.859636332	-0.00019706	0.00743749
m	-0.14910221	0.006828299	-21.8359213	-0.16249155	-0.13571287
n	0.065522	0.010532917	6.220688759	0.044868425	0.086175575
o	0.091919534	0.022155819	4.148776156	0.048475076	0.135363991
p	-0.01212048	0.001680868	-7.21084594	-0.01541643	-0.00882453
q	-0.08405668	0.003191254	-26.3397016	-0.09031428	-0.07779907
r	-0.0440042	0.010281602	-4.27989773	-0.06416499	-0.02384342
s	-0.06017752	0.023038296	-2.61206463	-0.10535239	-0.01500265
t	0.008757475	0.001696218	5.162942446	0.005431429	0.012083521
u	0.017513355	0.003938986	4.446157747	0.009789554	0.025237155
v	-0.00246993	0.012609082	-0.19588483	-0.02719457	0.022254716
aa	0.039002096	0.011544813	3.378322022	0.016364335	0.061639856
ab	-0.00074162	0.001851252	-0.40060613	-0.00437167	0.002888424
ac	0.015025465	0.002989386	5.026270728	0.009163697	0.020887233
ad	-0.01303295	0.015789574	-0.8254152	-0.0439941	0.017928188
ae	-0.02266373	0.010482884	-2.16197451	-0.0432192	-0.00210826
af	0.003886515	0.002080137	1.868393699	-0.00019234	0.007965373
ag	0.002488564	0.002923256	0.851298593	-0.00324353	0.008220659
ah	-0.03343191	0.014471965	-2.31011561	-0.06180941	-0.00505442
ai	0.015027731	0.005674328	2.648371854	0.003901168	0.026154294
aj	0.010053346	0.00173956	5.779245009	0.006642312	0.013464381
ak	-0.00084285	0.002736157	-0.30804099	-0.00620807	0.004522371
al	0.025920178	0.007873803	3.29195173	0.010480754	0.041359602
am	-0.01021499	0.005263174	-1.94084257	-0.02053534	0.000105355

Figure 11.5: Shuttle lift coefficients for Eqn1408 Chebyshev fit.

Parm	Value	Std Error	t-value	95.00% Confidence Limits		P>|t|
a	0.180350203	0.00187452	96.21139777	0.176874512	0.184025895	0.00000
b	0.015777855	0.002555855	6.173219832	0.010766154	0.020789556	0.00000
c	-0.14117249	0.002630856	-53.6602892	-0.14633125	-0.13601372	0.00000
d	0.012489176	0.00241376	5.174158753	0.007756106	0.017222247	0.00000
e	-0.12018653	0.003575941	-33.6097605	-0.12719848	-0.11317457	0.00000
f	0.146169872	0.00260136	56.18979678	0.141068943	0.151270802	0.00000
g	0.00739936	0.002651892	2.790218905	0.002199343	0.012599377	0.00531
h	-0.06015518	0.003387109	-17.7600351	-0.06679686	-0.0535135	0.00000
i	0.017290611	0.003572302	4.84018705	0.010285789	0.024295433	0.00000
j	0.130692873	0.002601385	50.23965781	0.125591887	0.135793859	0.00000
k	0.002943652	0.002589756	1.136652554	-0.00213452	0.008021828	0.25579
l	-0.02927995	0.003715334	-7.88083856	-0.03656524	-0.02199466	0.00000
m	0.013988855	0.003383058	4.134972904	0.007355115	0.020622595	0.00004
n	0.116630677	0.00352408	33.09535467	0.109720412	0.123540941	0.00000
o	-0.04249767	0.002593234	-16.387906	-0.04758267	-0.03741268	0.00000
p	-0.00095251	0.002620115	-0.36353743	-0.00609022	0.004185196	0.71623
q	-0.00275526	0.00363041	-0.75893806	-0.00987402	0.004363507	0.44796
r	0.009173683	0.00371439	2.469768126	0.001890244	0.016457122	0.01358
s	0.059286459	0.003382564	17.52707789	0.05265389	0.065919229	0.00000
t	0.000746732	0.003520392	0.212116208	-0.0061563	0.007649764	0.83203
u	0.016497623	0.00258834	6.373824935	0.011422224	0.021573022	0.00000
v	-0.00442101	0.002608255	-1.69500468	-0.00953546	0.000693446	0.09019
aa	0.008523515	0.003672295	2.321029357	0.001322611	0.015724418	0.02036
ab	0.004400011	0.003619247	1.215725382	-0.00269686	0.011496885	0.22420
ac	0.031839871	0.003708512	8.585618665	0.024567959	0.039111783	0.00000
ad	0.000749394	0.003316436	0.225963654	-0.00575371	0.007252495	0.82125
ae	0.020737259	0.003480433	5.958240387	0.01391258	0.027561939	0.00000
af	0.001630323	0.002566612	0.635204099	-0.00340247	0.006663117	0.52535
ag	-0.00650794	0.002457334	-2.64837517	-0.01132646	-0.00168943	0.00814
ah	0.021325047	0.003635677	5.865495677	0.014195955	0.028454139	0.00000
ai	-0.00292258	0.003550086	-0.82324228	-0.00988384	0.004038678	0.41045
aj	-0.00196076	0.003562479	-0.55039264	-0.00894632	0.005024798	0.58210
ak	0.000932405	0.003634412	0.256549053	-0.00619421	0.008059015	0.79755
al	0.005115264	0.003274113	1.562336045	-0.00130485	0.011535375	0.11833
am	0.000102125	0.003461184	0.029505911	-0.00668481	0.006889058	0.97646
an	-0.01671263	0.002512764	-6.65109518	-0.02163984	-0.01178543	0.00000
ao	-0.00589506	0.002669786	-2.20806488	-0.01113017	-0.0006599	0.02733
ap	0.025111168	0.003438841	7.302219304	0.018368047	0.031854289	0.00000
aq	-0.00509515	0.003636116	-1.40126119	-0.0122251	0.002034805	0.16125
ar	-0.01650054	0.003548566	-4.64991819	-0.02345882	-0.00954226	0.00000
as	0.000841139	0.003559574	0.236303319	-0.00613872	0.007821002	0.81322
at	-0.00125134	0.00362722	-0.34498684	-0.00836385	0.005861165	0.73013
au	5.03618e-06	0.003273512	0.001538462	-0.0064139	0.006423969	0.99877
av	-0.0256722	0.003451854	-7.43722026	-0.03244084	-0.01890356	0.00000
ba	-0.00054211	0.002511376	-0.21586239	-0.00546659	0.004382371	0.82911
bb	-0.00824564	0.002387109	-3.4542391	-0.01292646	-0.00356483	0.00056
bc	0.024826206	0.003680696	6.744976382	0.017608838	0.032043574	0.00000
bd	-0.00834879	0.003418778	-2.44203953	-0.01505257	-0.00164501	0.01467
be	-0.02866065	0.00354041	-8.09529199	-0.03560294	-0.02171837	0.00000
bf	0.000738957	0.003505759	0.210783636	-0.00613538	0.007613295	0.83307
bg	-0.0028907	0.003492098	-0.8277844	-0.00973826	0.003956848	0.40787
bh	-4.3068e-05	0.003595326	-0.01197889	-0.00709304	0.007006902	0.99044
bi	-0.00548911	0.003257526	-1.68505525	-0.0118767	0.000898475	0.09210
bj	-4.9573e-05	0.003316351	-0.014948	-0.00655251	0.006453362	0.98807
bk	0.019221637	0.002471283	7.777997862	0.01437577	0.024067503	0.00000
bl	-0.00736668	0.00201716	-3.65200468	-0.01132207	-0.00341129	0.00027
bm	0.027070928	0.003241702	8.350839283	0.020714371	0.033427485	0.00000
bn	-0.01384999	0.003244266	-4.26906689	-0.02021157	-0.0074884	0.00002
bo	-0.04305194	0.003060377	-14.0675284	-0.04905294	-0.03705093	0.00000
bp	0.000614432	0.003102744	0.198028525	-0.00546965	0.00669851	0.84304
bq	-0.00696332	0.003022715	-2.30366408	-0.01289047	-0.00103617	0.02132
br	-1.3738e-05	0.0031873	-0.00431013	-0.00626362	0.006236144	0.99656
bs	0.005998417	0.00329141	1.82244592	-0.00045561	0.012452446	0.06850
bt	1.21752e-05	0.003015388	0.004037698	-0.00590061	0.005924961	0.99678
bu	0.026556173	0.002827055	9.393567222	0.021012676	0.032099671	0.00000
bv	-0.00051493	0.001619521	-0.31795135	-0.0036906	0.002660742	0.75055

Figure 11.6: Shuttle moment coefficients for Eqn539 cosine fit.

Equations 1401-1410: Chebyshev Series Rationals
x' x scaled -1 to +1
y' y scaled -1 to +1
$T_n(x') = \cos(n\arccos(x'))$

$$1408 \quad z = (a + dT_1(x') + eT_1(y') + hT_2(x') + iT_2(y') + lT_3(x') + mT_3(y') + pT_4(x') + qT_4(y') + tT_5(x') + uT_5(y') + abT_6(x') + acT_6(y') + afT_7(x') + agT_7(y') + ajT_8(x') + akT_8(y'))/$$
$$(1 + bT_1(x') + cT_1(y') + fT_2(x') + gT_2(y') + jT_3(x') + kT_3(y') + nT_4(x') + oT_4(y') + rT_5(x') + sT_5(y') + vT_6(x') + aaT_6(y') + adT_7(x') + aeT_7(y') + ahT_8(x') + aiT_8(y') + alT_9(x') + amT_9(y'))$$

Figure 11.7: Chebyshev Eqn1408.

Equations 521-524: Fourier Series Bivariate Polynomials
x" x scaled 0 to π
y" y scaled 0 to π

524 $z=a+b\cos(x")+c\cos(y")+d\sin(x")+e\sin(y")+f\cos(2x")+g\cos(2y")+h\sin(2x")+i\sin(2y")+$
$j\cos(3x")+k\cos(3y")+l\sin(3x")+m\sin(3y")+n\cos(4x")+o\cos(4y")+p\sin(4x")+q\sin(4y")+$
$r\cos(5x")+s\cos(5y")+t\sin(5x")+u\sin(5y")+$
$v\cos(x")\cos(y")+aa\cos(x")\sin(y")+ab\sin(x")\cos(y")+ac\cos(x")\cos(2y")+$
$ad\cos(2x")\cos(y")+ae\cos(x")\sin(2y")+af\sin(3x")\cos(y")+ag\cos(x")\cos(3y")+$
$ah\cos(3x")\cos(y")+ai\cos(x")\sin(3y")+aj\sin(3x")\cos(y")+ak\cos(x")\cos(4y")+$
$al\cos(4x")\cos(y")+am\cos(x")\sin(4y")+an\sin(4x")\cos(y")+ao\sin(x")\sin(y")+$
$ap\sin(x")\cos(2y")+aq\cos(2x")\sin(y")+ar\sin(x")\sin(2y")+as\sin(2x")\sin(y")+$
$at\sin(x")\cos(3y")+au\cos(3x")\sin(y")+av\sin(x")\sin(3y")+ba\sin(3x")\sin(y")+$
$bb\sin(x")\cos(4y")+bc\cos(4x")\sin(y")+bd\sin(x")\sin(4y")+be\sin(4x")\sin(y")+$
$bf\cos(2x")\cos(2y")+bg\cos(2x")\sin(2y")+bh\sin(2x")\cos(2y")+bi\cos(2x")\cos(3y")+$
$bj\cos(3x")\cos(2y")+bk\cos(2x")\sin(3y")+bl\sin(3x")\cos(2y")+bm\sin(2x")\sin(2y")+$
$bn\sin(2x")\cos(3y")+bo\cos(3x")\sin(2y")+bp\sin(2x")\sin(3y")+bq\sin(3x")\sin(2y")$

Figure 11.8: Fourier Eqn524.

Equations 531-539: Cosine Series Bivariate Polynomials
x" x scaled 0 to π
y" y scaled 0 to π

539 $z=a+b\cos(x")+c\cos(y")+d\cos(2x")+e\cos(x")\cos(y")+f\cos(2y")+$
$g\cos(3x")+h\cos(2x")\cos(y")+i\cos(x")\cos(2y")+j\cos(3y")+$
$k\cos(4x")+l\cos(3x")\cos(y")+m\cos(2x")\cos(2y")+n\cos(x")\cos(3y")+o\cos(4y")+$
$p\cos(5x")+q\cos(4x")\cos(y")+r\cos(3x")\cos(2y")+s\cos(2x")\cos(3y")+t\cos(x")\cos(4y")+u\cos(5y")+$
$v\cos(6x")+aa\cos(5x")\cos(y")+ab\cos(4x")\cos(2y")+ac\cos(3x")\cos(3y")+ad\cos(2x")\cos(4y")+ae\cos(x")+\cos(5y")+$
$af\cos(6y")+$
$ag\cos(7x")+ah\cos(6x")\cos(y")+ai\cos(5x")\cos(2y")+aj\cos(4x")\cos(3y")+ak\cos(3x")\cos(4y")+al\cos(2x")\cos(5y")+$
$am\cos(x")\cos(6y")+an\cos(7y")+$
$ao\cos(8x")+ap\cos(7x")\cos(y")+aq\cos(6x")\cos(2y")+ar\cos(5x")\cos(3y")+as\cos(4x")\cos(4y")+at\cos(3x")\cos(5y")+$
$au\cos(2x")\cos(6y")+av\cos(x")\cos(7y")+ba\cos(8y")+$
$bb\cos(9x")+bc\cos(8x")\cos(y")+bd\cos(7x")\cos(2y")+be\cos(6x")\cos(3y")+bf\cos(5x")\cos(4y")+bg\cos(4x")\cos(5y")+$
$bh\cos(3x")\cos(6y")+bi\cos(2x")\cos(7y")+bj\cos(x")\cos(8y")+bk\cos(9y")+$
$bl\cos(10x")+bm\cos(9x")\cos(y")+bn\cos(8x")\cos(2y")+bo\cos(7x")\cos(3y")+bp\cos(6x")\cos(4y")+bq\cos(5x")\cos(5y")+$
$br\cos(4x")\cos(6y")+bs\cos(3x")\cos(7y")+bt\cos(2x")\cos(8y")+bu\cos(x")\cos(9y")+bv\cos(10y")$

Figure 11.9: Cosine Eqn539

Equations 601-609: Sigmoid Series Bivariate Polynomials
x' x scaled -1 to +1
y' y scaled -1 to +1
$S_{i=2..n}(x') = -1+2/(1+\exp(-(x'+1-(i-1)*(2/n))/0.12))$, $S_1(x') = x'$

608 $z=a+bS_1(x')+cS_1(y')+dS_2(x')+eS_1(x')S_1(y')+fS_2(y')+gS_3(x')+hS_2(x')S_1(y')+iS_1(x')S_2(y')+jS_3(y')+$
$kS_4(x')+lS_3(x')S_1(y')+mS_2(x')S_2(y')+nS_1(x')S_3(y')+oS_4(y')+$
$pS_5(x')+qS_4(x')S_1(y')+rS_3(x')S_2(y')+sS_2(x')S_3(y')+tS_1(x')S_4(y')+uS_5(y')+$
$vS_6(x')+aaS_5(x')S_1(y')+abS_4(x')S_2(y')+acS_3(x')S_3(y')+adS_2(x')S_4(y')+aeS_1(x')S_5(y')+afS_6(y')+$
$agS_7(x')+ahS_6(x')S_1(y')+aiS_5(x')S_2(y')+ajS_4(x')S_3(y')+akS_3(x')S_4(y')+alS_2(x')S_5(y')+amS_1(x')S_6(y')+anS_7(y')+$
$aoS_8(x')+apS_7(x')S_1(y')+aqS_6(x')S_2(y')+arS_5(x')S_3(y')+asS_4(x')S_4(y')+atS_3(x')S_5(y')+auS_2(x')S_6(y')+avS_1(x')S_7(y')+baS_8(y')+$
$bbS_9(x')+bcS_8(x')S_1(y')+bdS_7(x')S_2(y')+beS_6(x')S_3(y')+bfS_5(x')S_4(y')+bgS_4(x')S_5(y')+bhS_3(x')S_6(y')+biS_2(x')S_7(y')+$
$bjS_1(x')S_8(y')+bkS_9(y')$

Figure 11.10: Sigmoid Eqn608.

83